

Aragonite–calcite veins of the ‘Erzberg’ iron ore deposit (Austria): Environmental implications from young fractures

RONNY BOCH*, XIANFENG WANG†, TOBIAS KLUGE‡, ALBRECHT LEIS§, KE LIN†, HANNES PLUCH¶, FLORIAN MITTERMAYR**, ANDRE BALDERMANN*, MICHAEL E. BÖTTCHER†† and MARTIN DIETZEL*

*Institute of Applied Geosciences, Graz University of Technology & NAWI Graz GeoCenter, Rechbauerstr. 12, 8010 Graz, Austria (E-mail: ronny.boch@tugraz.at)

†Earth Observatory of Singapore and Asian School of the Environment, Nanyang Technological University, 50 Nanyang Avenue, 639798 Singapore, Singapore

‡Institute of Environmental Physics, University of Heidelberg, Im Neuenheimer Feld 229, 69120 Heidelberg, Germany

§JR-AquaConSol GmbH, Steyrergasse 21, 8010 Graz, Austria

¶VA Erzberg GmbH, Erzberg 1, 8790 Eisenerz, Austria

**Institute of Technology & Testing of Building Materials, Graz University of Technology, Inffeldgasse 24, 8010 Graz, Austria

††Geochemistry & Isotope Biogeochemistry Unit, Leibniz Institute for Baltic Sea Research (IOW), Seestr. 15, 18119 Warnemünde, Germany

Associate Editor – Alexander Brasier

ABSTRACT

The well-known Erzberg site represents the largest siderite (FeCO_3) deposit in the world. It consists of various carbonates accounting for the formation of prominent CaCO_3 (dominantly aragonite) precipitates filling vertical fractures of different width (centimetres to decimetres) and length (tens of metres). These commonly laminated precipitates are known as ‘erzbergite’. This study focuses on the growth dynamics and environmental dependencies of these vein fillings. Samples recovered on-site and from mineral collections were analyzed, and these analyses were further complemented by modern water analyses from different Erzberg sections. Isotopic signatures support meteoric water infiltration and sulphide oxidation as the principal hydrogeochemical mechanism of (Ca, Mg and Fe) carbonate host rock dissolution, mobilization and vein mineralization. Clumped isotope measurements revealed cool formation temperatures of *ca* 0 to 10°C for the aragonite, i.e. reflecting the elevated altitude Alpine setting, but unexpectedly low for aragonite nucleation. The ^{238}U – ^{234}U – ^{230}Th dating yielded ages from 285.1 ± 3.9 to 1.03 ± 0.04 kyr BP and all samples collected on-site formed after the Last Glacial Maximum. The observed CaCO_3 polymorphism is primarily controlled by the high aqueous Mg/Ca ratios resulting from dissolution of Mg-rich host rocks, with Mg/Ca further evolving during prior CaCO_3 precipitation and CO_2 outgassing in the fissured aquifer. Aragonite represents the ‘normal’ mode of erzbergite formation and most of the calcite is of diagenetic (replacing aragonite) origin. The characteristic lamination (millimetre-scale) is an original growth feature and mostly associated with the deposition of stained (Fe-rich) detrital particle layers. Broader zonations (centimetre-scale) are commonly of diagenetic origin. Petrographic observations and radiometric dating support an irregular nature for most of the layering. Open fractures resulting from fault tectonics or gravitational mass movements provide water flow routes and fresh chemical reaction surfaces

of the host rock carbonates and accessory sulphides. If these prerequisites are considered, including the hydrogeochemical mechanism, modern water compositions, young U-Th ages and calculated precipitation rates, it seems unlikely that the fractures had stayed open over extended time intervals. Therefore, it is most likely that they are geologically young.

Keywords Aragonite, carbonate precipitates, clumped isotopes, Erzberg, radiometric U-Th dating, siderite, sulphide oxidation, vein.

INTRODUCTION

The ‘Erzberg’ iron ore deposit represents the largest siderite (FeCO_3) occurrence worldwide and is amongst Austria’s most prominent geological places due to its historic, economic and scientific value. Local carbonate host rocks of variable chemistry and alteration host prominent CaCO_3 (aragonite and calcite) precipitates infilling vertical fractures of different width (centimetres to decimetres) and length (tens of metres). These often laminated and visually attractive carbonate precipitates are referred to as ‘erzbergite’ in mineral collections and decorative contexts. Aside from the iron ore carbonates siderite and ankerite, the erzbergite occurrences have been the subject of early scientific discussion (Hatle, 1892; Angel, 1939). These pioneering authors conducted investigations on the aragonite versus calcite relation and the possibility of a regular annual lamination pattern. Further, they discussed the rare occurrences of ‘Eisenblüte’ (iron flower), i.e. typically dendritic (resembling tree branches) and fragile mineral formations in some fractures consisting exclusively of aragonite (Hatle, 1892; Angel, 1939). The latter are closely associated with more extensive erzbergite precipitates and in some aspects (dendritic, channels inside) they are comparable to eccentricities (helictites) in karst caves (Onuk *et al.*, 2014). Similarly, the erzbergite fracture fillings show analogies with flowstone formations precipitating from CaCO_3 supersaturated aqueous solutions (vadose waters) flowing across walls and floors in cave systems of differing depths underground (Fairchild *et al.*, 2006). An increasing number of studies focused on a better understanding of flowstone growth dynamics and their potential application as chemical–sedimentary archives in order to reconstruct changing environmental conditions, such as past temperatures and meteoric precipitation (Drysdale *et al.*, 2006; Boch & Spötl, 2011), mountain uplift rates (Meyer *et al.*, 2011) or aragonite versus calcite

precipitation (Spötl *et al.*, 2016). This study presumes that the aragonite–calcite successions in fractures at Erzberg hold a similar potential with regard to specific palaeoenvironmental information. Understanding their mineralogical and hydrogeochemical formation conditions, however, is a prerequisite for reliable interpretations of growth dynamics and (palaeo)environmental variability.

This study investigated selected representative erzbergite samples from mineral collections and from fractures currently accessible at Erzberg. For the first time, radiometric dating of this material was conducted, and genetic aspects were evaluated in detail. The latter included high spatial (temporal) resolution petrographic analysis, elemental content and distribution, as well as stable (C and O) and clumped isotope measurements. In addition, local waters from different sections of the open pit mine were analyzed for their major and trace elemental, as well as stable isotopic (H, C, O and S) compositions. The new results shed light onto the formation conditions of the aragonite–calcite vein precipitates in relation to siderite–ankerite and environmental parameters.

SETTING AND SAMPLING

At Erzberg near Eisenerz (Styria, Austria; Fig. 1), early mining activities might trace back to Celtic and Roman times (Schulz *et al.*, 1997; Prochaska, 2012). Since 1928, the locally extensive Fe-rich mountain range was strongly modified as the result of mining activity (1532 m originally; 1466 m above sea-level today). It consists of 30 successive stages (berms), 24 m high, resulting in the characteristic pyramid shape of the current open pit mine (Fig. 1). About 25% (up to three million metric tons per year) of iron ore processed by the Voest–Alpine steel industry (in Linz and Donawitz) is produced from this mine, i.e. *ca*

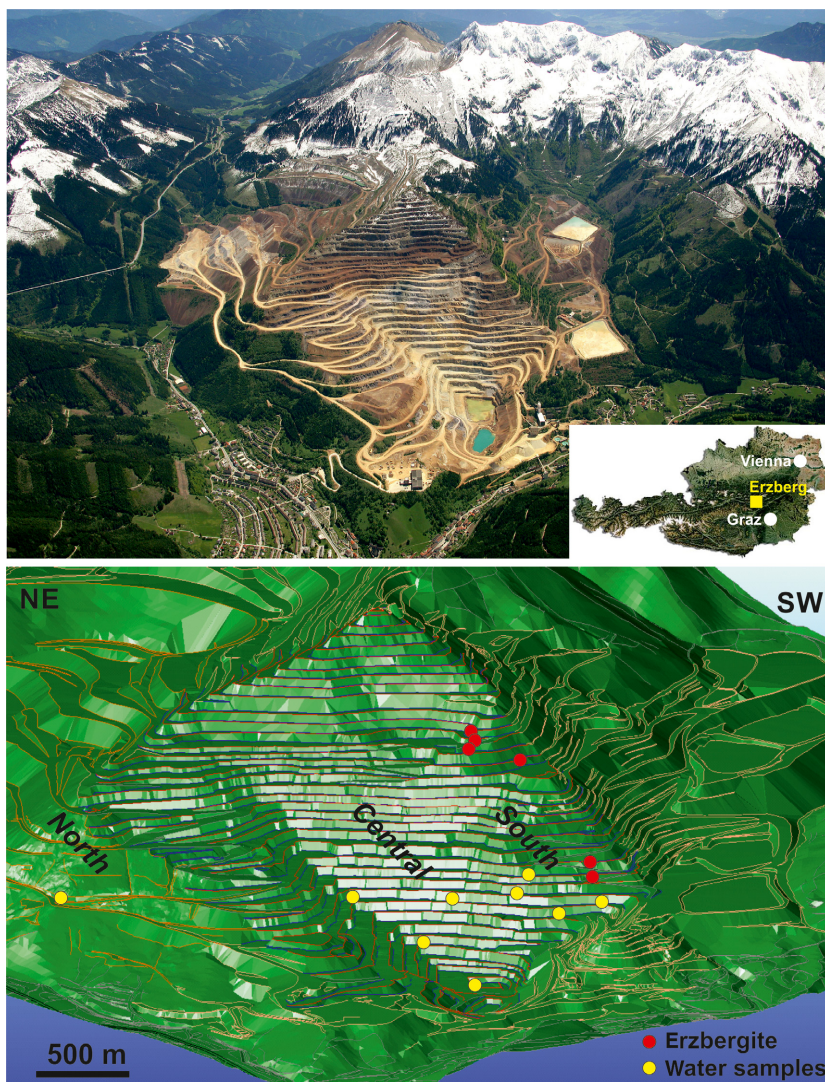


Fig. 1. Aerial overview of the Erzberg open pit iron ore mine. Upper image (photograph credit; Bavaria Luftbild Verlags GmbH): The inset shows the location in the region of Styria, Austria (yellow square). Lower image: Digital surface model of Erzberg displaying the positions of sampled carbonate precipitates in fractures (erzbergite) and aqueous solution samples (fracture and surface waters).

245 million metric tons to date and future reserves of *ca* 150 million metric tons (Prochaska, 2012). Regarding the regional geology, this major ore deposit is part of the Noric nappe system within the Greywacke unit at the base of the Northern Calcareous Alps (Schönlaub, 1982; Schmid *et al.*, 2004; Bryda *et al.*, 2013). The complex sedimentary and tectonic evolution is marked by Variscan nappe stacking of Silurian/Devonian limestones and Carboniferous (dark siliceous) schists, as well as subsequent discordant transgression (Permo-Triassic) and Alpine tectonic synclinal deformation (Cretaceous). The interrelated siderite and ankerite $[(Ca,Fe,Mg)_2(CO_3)_2]$ iron ore is hosted by Devonian limestones/marbles (lower greenschist facies; Prochaska, 2016). Next to the dominant calcium carbonates

(calcitic limestone) and iron ore carbonates (siderite and ankerite), associated quartz, muscovite/sericite and various accessory sulphide minerals (pyrite, chalcopyrite, arsenopyrite, sphalerite, galenite, fahlore and cinnabar) are widespread (Thalman, 1979; Schulz *et al.*, 1997; Prochaska, 2012).

To study the specific formation conditions and (palaeo)environmental controls of erzbergite in vertical fractures dissecting Erzberg, aragonite–calcite samples were recovered on-site, from currently accessible rare veins that measure centimetres to decimetres horizontally and often tens of metres in vertical extension (Fig. 2). Sample material from the Graz University of Technology (Styria, Austria) collection and private collectors were also investigated. The thickness of the individual samples typically reflects

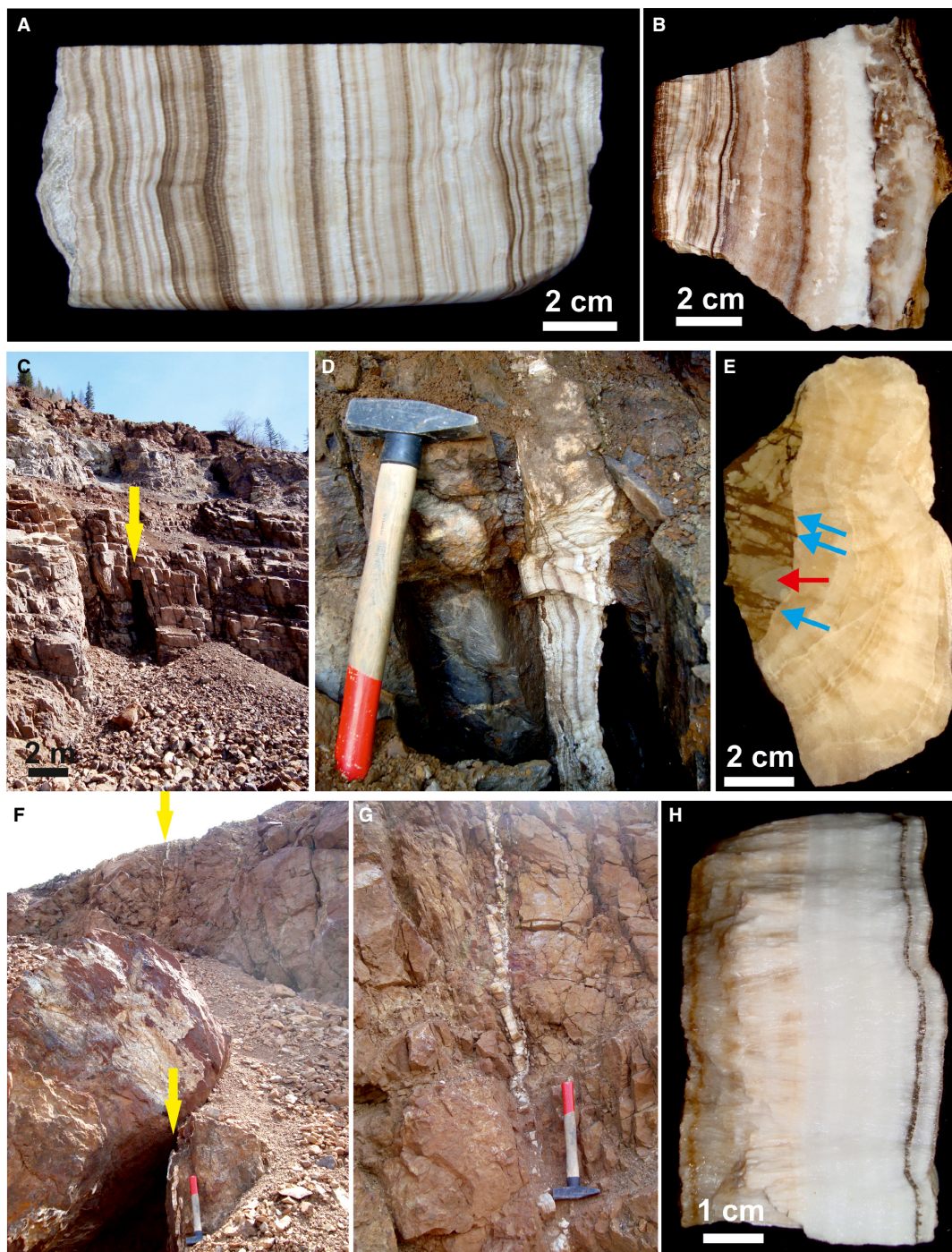


Fig. 2. Field impressions from the Erzberg mine and selected samples of erzbergite (aragonite–calcite) fracture fillings. (A) Well-laminated erzbergite from a private collection (sample EB1). (B) Typically laminated (millimetre-scale) and banded (centimetre-scale) erzbergite precipitate collected on-site and showing some distinct macroscopic features of aragonite (snow white) to calcite (beige) transformation. (C) and (D) Major fracture (arrow) filled with laminated and unidirectional aragonite–calcite precipitates (sample EB6; ca 10 cm thick). Hammer for scale is 33 cm long. (E) Dominantly calcitic, beige coloured and layered erzbergite sample (EB22) recovered on-site. This sample includes part of the local ankerite host rock (greyish, red arrow) dissected by several red-brownish veins consisting of Mg-calcite and goethite (blue arrows). (F) and (G) Extensive vertical fracture (arrows) completely filled with precipitated calcium carbonate of almost pure aragonitic (H) composition (sample EB7 from upper part of the fracture).

the width of the respective fracture, and most samples show remains of host rock components (fracture wall) at their base and top. In addition, some of the typical Erzberg host rocks (siderite, ankerite and limestone) were collected. Modern water samples were collected on-site in July 2015 and April 2016 from nine different places constrained by GPS data (Fig. 1), i.e. mostly small water flows along fractures or surfaces existing and accessible in order to conduct hydrochemical analyses and aqueous solution modeling.

METHODS

Solid phases

The mineralogy and petrography (lamination and fabric) of erzbergite precipitates were analyzed using polished, non-covered thin-sections for transmitted and reflected light microscopy (Leica DMLP Polarizing Microscope; Leica, Wetzlar, Germany) connected to an Olympus DP26 camera (Olympus, Tokyo, Japan). Aliquots (*ca* 0.5 g) of erzbergite and adjacent host rock samples were used for powder X-ray diffraction analysis (XRD) in order to determine their mineralogical compositions qualitatively and semi-quantitatively. A PANalytical (Almelo, The Netherlands) X'Pert PRO diffractometer equipped with a Co-K α X-ray radiation source (40 mA, 40 kV), an X'Celerator detector and measurement parameters of 4 to 85° 2θ -range, 0.01° step propagation (2θ) and 40 sec per step counting time were applied. Diffraction patterns were evaluated using the software PANalytical HighScore Plus (version 3.0d). High spatial (temporal) resolution major and minor elemental distributions (wavelength-dispersive mapping mode; WDX) and back-scattered electron images (BSE) of selected erzbergite samples were analyzed on polished thick sections using a JEOL JXA-8200 electron microprobe (EPMA, Tokyo, Japan). Elemental distribution images of Ca, Mg, Fe, Si and Al were recorded with an accelerating voltage of 15 kV, beam current of 30 nA and *ca* 1 μ m electron beam resolution. 800 \times 600 or 800 \times 800 point analyses, a step size of 1.5 to 3.0 μ m and a counting time of 6 to 12 msec per step yielded elemental distribution maps of 2400 \times 1800 and 1200 \times 1200 μ m for two different erzbergite samples (EB3 and EB2), respectively. In addition, spot analyses of selected calcites were conducted in WDX mode and

calibrated against dolomite (Mg) and calcite (Ca) mineral standards in order to quantify the Mg concentration and Mg/Ca ratio.

Isotopic analyses included the first ^{234}U – ^{230}Th radiometric age determinations of erzbergite CaCO_3 samples. Depending on the particular sample, either only the growth inception [at one or both fracture walls, i.e. the sample base(s)] and growth cessation [mostly complete fracture filling, i.e. sample top(s)] or multiple subsamples across the respective carbonate precipitate growth axis were measured. Small sample aliquots (few tens of milligrams of powder) were milled along growth layers using a tungsten-carbide handheld drill or were cut (slices) using a diamond-coated circular saw. After acid digestion of the carbonate the relevant uranium and thorium contents were separated and purified using ion-exchange resin in columns following chemical protocols described in Cheng *et al.* (2013). The U and Th isotope ratios for age determination were measured via a Thermo Fisher Scientific Neptune Plus Multicollector ICP–MS (inductively coupled plasma – mass spectrometer; Thermo Fisher Scientific, Waltham, MA, USA) at the Earth Observatory of Singapore, Nanyang Technological University (Wang *et al.*, 2017). Absolute U–Th ages were calculated using the decay constants of ^{234}U and ^{230}Th reported in Cheng *et al.* (2013) and the measured ages were corrected using a bulk earth atomic ratio of 4.4 ± 2.2 ppm for initial $^{230}\text{Th}/^{232}\text{Th}$. The final isotopic and age uncertainties are quoted at the 2σ -level. Typical relative age uncertainties of the analyzed erzbergite precipitates are in the range of 0.3 to 1.5%, mainly depending on U concentrations and ages of the samples.

Stable C and O isotope compositions of aragonite and calcite (erzbergite), as well as of host rock carbonates (siderite, ankerite and limestone calcite) were determined by the methods described in Dietzel *et al.* (2015). Powdered aliquots (0.3 to 0.6 mg) were extracted pointwise across the profiles of erzbergite samples using a handheld drill and, in the case of sample EB2, using an ESI New Wave Research (Portland, OR, USA) computer-controlled micromill device. The latter was deployed to produce a continuous and high spatial resolution isotope transect (Spötl & Matthey, 2006). The stable C and O isotopic compositions of the carbonates were measured by continuous-flow isotope-ratio mass-spectrometry applying a Thermo Fisher Scientific GasBench II connected to a Finnigan

Delta^{plus} XP mass spectrometer (Thermo Fisher Scientific). Oxygen isotope data of siderite and ankerite were corrected for mineral specific phosphoric acid fractionation (Rosenbaum & Sheppard, 1986; Kim *et al.*, 2015). Measured isotope ratios are given relative to the Vienna Pee-Dee Belemnite (VPDB) reference and typical analytical precision (2σ) is ± 0.1 and $\pm 0.08\text{‰}$ for the $\delta^{13}\text{C}$ and $\delta^{18}\text{O}$ values, respectively (Dietzel *et al.*, 2015).

Clumped isotope (multiply-substituted isotopologues; Eiler, 2007; Huntington & Lechler, 2015) measurements were conducted for selected erzbergite aragonite samples. This stable isotope thermometer is based on a homogeneous (single phase) isotope exchange and the measurement of the rare ^{13}C and ^{18}O isotopes bonded together in a carbonate molecule ($^{13}\text{C}^{18}\text{O}^{16}\text{O}_2^{2-}$). Analytically, drilled subsample powders of 2 to 6 mg were reacted with *ca* 1 ml of 105% phosphoric acid in stirred glass vessels at 90°C for 10 min and the released CO_2 was collected in a nitrogen-cooled glass trap (Kluge *et al.*, 2015). After separation (for example, from H_2O) and purification the evolved and cryogenically trapped CO_2 was transferred either to a Finnigan MAT 253 stable isotope ratio mass spectrometer (Thermo Fisher Scientific) at Imperial College, London; or a Finnigan MAT 253 Plus (Thermo Fisher Scientific) at Heidelberg University for immediate carbonate clumped isotope analysis. A typical measurement consisted of three to four acquisitions with 10 cycles per acquisition. The clumped isotopic composition is plotted as Δ_{47} value, i.e. the deviation of the measured ^{13}C – ^{18}O abundance from stochastic distribution at very high temperature; Δ_{47} then increases with decreasing temperature. The data evaluation follows the procedures described by Dennis *et al.* (2011) and includes gas and carbonate standards as reference, as well as the ^{17}O correction of Daëron *et al.* (2016). For final temperature calculation, the experimental Δ_{47} versus temperature relationship published in Kluge *et al.* (2015) was adopted.

Aqueous solution

During two field campaigns water temperature (°C), electrical conductivity (EC; $\mu\text{S cm}^{-1}$) and pH were measured using a WTW Multi350i combi instrument equipped with SenTix41 and TetraCon325 electrodes (WTW, Weilheim, Germany). Samples for chemical and stable isotopic

analyses were pre-treated (0.45 μm filtered, acidified) and bottled. The water analyses in field and laboratory followed the procedures and instrumentation reported in Boch *et al.* (2015). Samples for the major cations and anions in solution were collected in completely filled gas-tight borosilicate bottles and quantified using a Dionex (Sunnyvale, CA, USA) ICS-3000 ion chromatograph (analytical error $< \pm 3\%$). The subsamples for carbonate alkalinity (expressed as HCO_3^-) were recovered in gas-tight containers and measured potentiometrically on the same day using a Schott (Mainz, Germany) TA20plus titrator adding 0.02 M HCl. Minor and trace element contents in aqueous solution (acidified) were determined with a Optima 8300 DV ICP–OES (optical emission spectrometry) (PerkinElmer, Waltham, MA, USA) calibrated by NIST 1640a standards (analytical error $< \pm 5\%$). Hydrochemical modelling based on the measured water parameters was performed using the PHREEQC computer code (version 3.2.0, wateq4f.dat database; Parkhurst & Appelo, 2013). This included the calculation of ion activities and speciation, mineral saturation states (SI values defined as ion activity product versus solubility product on a logarithmic scale, i.e. $\text{SI} = \log [\text{IAP}/\text{K}_{\text{sp}}]$, $\text{SI} = 0$ means saturation), as well as aqueous solution CO_2 partial pressures (internal P_{CO_2}).

Stable isotope analyses of the collected waters comprised their hydrogen ($\delta^2\text{H}$) and oxygen ($\delta^{18}\text{O}$) isotopic composition, carbon isotopes of dissolved inorganic carbon ($\delta^{13}\text{C}_{\text{DIC}}$) and sulphur isotopes of dissolved sulphate ($\delta^{34}\text{S}_{\text{SO}_4}$). The $\delta^2\text{H}$ values were analyzed with a continuous-flow mass spectrometer (Finnigan Delta^{plus} XP; Thermo Fisher Scientific) applying the chromium reduction technique and the $\delta^{18}\text{O}$ values were determined mass spectrometrically using the traditional CO_2 – H_2O equilibration technique (Horita *et al.*, 1989; Morrison *et al.*, 2001). Typical analytical precisions (1σ) are $\pm 0.8\text{‰}$ for $\delta^2\text{H}$ and $\pm 0.05\text{‰}$ for $\delta^{18}\text{O}$ and the values are referenced relative to the Vienna Standard Mean Ocean Water (VSMOW) standard. The $\delta^{13}\text{C}_{\text{DIC}}$ values were determined following the sampling procedure and mass spectrometric analysis described in Spötl (2005). The C isotope ratios are reported relative to VPDB and analytical precision is better than $\pm 0.1\text{‰}$. $\delta^{34}\text{S}_{\text{SO}_4}$ values were measured on BaSO_4 precipitated from selected acidified aqueous solutions via the addition of $\text{Ba}(\text{Cl})_2$ solution. Mass spectrometric analyses were carried out at the Leibniz-Institut für

Ostseeforschung Warnemünde – IOW – on a Finnigan MAT 253 mass spectrometer coupled to a Thermo Flash 2000 elemental analyzer via a Thermo Finnigan Conflow III interface (Thermo Fisher Scientific) (Winde *et al.*, 2017). The measurements had typical analytical precisions of $\pm 0.2\text{‰}$ and the data are reported relative to the Vienna Canyon Diablo Troilite (VCDT) reference scale following the procedures described by Mann *et al.* (2009).

Modern waters from Erzberg and erzbergite carbonate stable isotopic compositions were also evaluated in comparison with instrumental meteorological data from the nearby Wildalpen [(610 m above sea-level (m a.s.l.))] meteorological station, 15 km from Erzberg, Styria (Umweltbundesamt, 2017). The data comprise available monthly averages of principal atmospheric parameters (air temperature in °C, precipitation sums in millimetres) and monthly stable H and O isotope values of regional meteoric precipitation during the time interval from January 1976 to December 2015.

RESULTS

Mineralogy, chemical and petrographic characterization

Macroscopic visual inspection

Most of the samples show layering based on colour changes ranging from snow white to dark brown (Fig. 2). It is possible to distinguish between a typically narrow lamination [(sub)-millimetre-scale; for example, Fig. 2A] and some wider and more irregular banding (centimetre-scale zonation; Fig. 2B). The lamination and banding do not appear in strictly regular recurrence intervals and the layering seems highly variable between different samples. The erzbergite precipitates are mostly compact. Only a few samples show sections of increased primary (from growth) or secondary (from dissolution) porosity. Most hand specimens possess an undulating growth topography resulting from the spatially variable growth surfaces and growth progress during mineral precipitation from the water flow in vertical fractures. Several of the investigated erzbergite samples include adjacent parts of the fracture wall host rocks at their base and commonly on both sample ends, i.e. samples recovered from fractures entirely filled with carbonate precipitates. Depending on the localization (and probably amount) of past

water flow, indications of unidirectional or bidirectional growth are often visible, i.e. mineral precipitation progressing from one or both fracture walls. Moreover, several samples show macroscopic features of partial later-stage diagenetic alteration, i.e. successive transformation of snow white to more beige coloured carbonate layers and sections (Fig. 2B).

Mineralogy

X-ray diffraction analysis of subsamples allowed constraining of the dominant macroscopic observations (Table S1). In most erzbergite samples the two CaCO_3 polymorphs aragonite and calcite occur, although they vary spatially and quantitatively. Particular layers or sections (bands) are either dominated by aragonite or calcite. Macroscopically, aragonite always appears as snow white precipitate, while calcite is typically of beige to light brownish colour (for example, sample EB6 in Fig. 2B to D). Some erzbergite precipitates consist of more or less pure calcite (for example, sample EB22; Table S1; Fig. 2E). In contrast, other samples of several centimetres thickness consist of almost exclusively aragonite (for example, sample EB7; Table S1; Fig. 2F to H). In the frequent intervals characterized by thin dark brownish layers, accessory quartz, muscovite and goethite were detected (samples EB9, EB13 and EB18; Table S1). For example, a prominent and thick brownish stained layer subsampled from EB13 (Table S1) consisted of Mg-calcite with minor contributions of quartz, muscovite and goethite. Magnesium-calcite was repeatedly found in association with the brownish stained layers. In some cases, the powder XRD analyses of subsamples containing thin brown to greyish layers only revealed the presence of aragonite and/or calcite. The XRD measurements were also conducted on representative host rock (fracture wall) components. A widespread whitish to grey coloured and coarse crystalline component (sample SK2; Table S1) is comprised of calcite with little quartz and is thus identified as slightly metamorphosed Devonian limestone (Sauburger Kalk). Similarly, a white/greyish and sharp-edged host rock component adjacent to well-laminated erzbergite consisted of calcite with little SiO_2 (quartz; sample EB13_XRD2), i.e. local iron ore bearing limestone. Another host rock component of distinct greyish colouring closely related to erzbergite carbonate (sample EB22; Fig. 2E) yielded ankerite representing the original fracture wall. Prominent red-brownish and less consolidated

veins dissecting this iron ore component (ankerite of EB22) are composed of ankerite and Mg-calcite, as well as goethite (sample EB22_XRD2; Table S1).

Petrographic characterization

A detailed petrographic characterization was conducted by applying transmitted light and reflected light microscopy to a broad selection of erzbergite samples (Figs S1 and 3). The microscopic evaluation supports the common but highly variable occurrence of lamination mainly resulting from aragonite, calcite and intermittent light to dark brownish stained layers. In most specimens, aragonite is the dominant and unaltered CaCO_3 polymorph. The aragonite crystals are characterized by a radiating, fascicular fabric (Fig. 3A to F), i.e. fan-like bundles of acicular crystals, and show competitive growth and undulatory light extinction. Original calcite crystals typically display a columnar growth fabric, i.e. a pronounced length to width relation along the calcite *c*-axes (Figs 3A, 3B and S1A; see also Frisia, 2015). Depending on competitive growth and the degree of lateral coalescence of individual crystallites, a columnar compact versus columnar open calcite fabric can be distinguished (Kendall & Broughton, 1978; Frisia, 2015). The latter fabric results from an inter-crystalline (micro) porosity, i.e. linear pore spaces frequently hosting fluid inclusions. The unaltered calcite layers mostly consist of calcite crystals with similar overall orientation (competitive growth and geometric selection; Fig. 3B) and show uniform light extinction under crossed nicols of the microscope. The transitions from aragonite to calcite or vice versa are often gradual (Figs S1A and 3A). A major part of the calcite, however, is unequivocally of diagenetic (later stage) origin, i.e. aragonite is replaced by calcite (Fig. 3C and D). The phase transformation between the different CaCO_3 polymorphs is manifested in aragonitic remnants (patches of radiating, fascicular crystals) within large (millimetre-scale) replace calcite crystals (Fig. S1B and C). The latter forms a characteristic mosaic to microsparitic fabric frequently showing indicative triple junctions from CaCO_3 dissolution and re-precipitation (Frisia, 2015). Such diagenetic replacement of aragonite towards calcite is also expressed in variable orientations (*c*-axis) of neighbouring calcite crystals or in a preserved undulatory light extinction of these mosaic crystals.

Importantly, large sections and bands (centimetre-scale) of erzbergite can be affected by diagenetic replacement resulting in a coarse crystalline (sparitic) fabric. The transformation can also preferentially occur across original growth layers, i.e. some types of layering could be of diagenetic origin.

Next to the light-coloured aragonite versus calcite lamination and banding, the recurrent deposition of brownish stained layers is of crucial importance. These mostly distinct and only locally diffuse layers show dominant red-brownish colours in transmitted light but more variable colouring (yellowish to black) under reflected light (Fig. 3E to J). In relation to aragonite and calcite the stained layers occur either inter-crystalline or intra-crystalline, i.e. CaCO_3 crystal (re-)nucleation and growth was affected in some cases. In the case of strongly ‘contaminated’ (thicker brownish layers) erzbergite growth surfaces, continuous CaCO_3 crystallization might have been interrupted and re-nucleation (new crystallites) of aragonite or (Mg-) calcite may have occurred. In most cases, however, evidence for ongoing CaCO_3 crystal growth was observed (Fig. 3E and F). The stained layers often trace the idiomorphic (euhedral) shape of calcite (rhombohedral) or aragonite (fascicular curved) crystal terminations (Figs S1D, 3G and 3H). Also, the layer thicknesses and grain sizes are highly variable between different layers of a sample, between different erzbergite samples and even across a particular stained layer (Fig. 3E to I). In some of the samples multiple stained layers show regular and spatially narrow recurrence intervals (Fig. 3E and F). At inter-crystalline pores, preferential accumulation of grains was observed (Figs S1D, 3G and 3H). In accordance with XRD results, the differently coloured particles consist of siliceous minerals (quartz and muscovite) and iron (oxy)hydroxides (goethite). Rare golden coloured grains are indicative of iron-sulphides (pyrite; Figs S1E, S1F, 3I and 3J). Bidirectional growth, i.e. on both fracture walls towards complete fracture filling, is documented in a few cases (samples EB2, EB9 and EB24; Fig. S1G). Sample EB1 locally exhibits irregular pore spaces of large but variable size/shape probably resulting from carbonate dissolution (Fig. S1H). These pores are typically associated with small ruptures in the brittle erzbergite. Two samples (EB10 and EB19) display scarce remnants of filamentous structures that could be some evidence of (local) microbial influence (Fig. S1I and J).

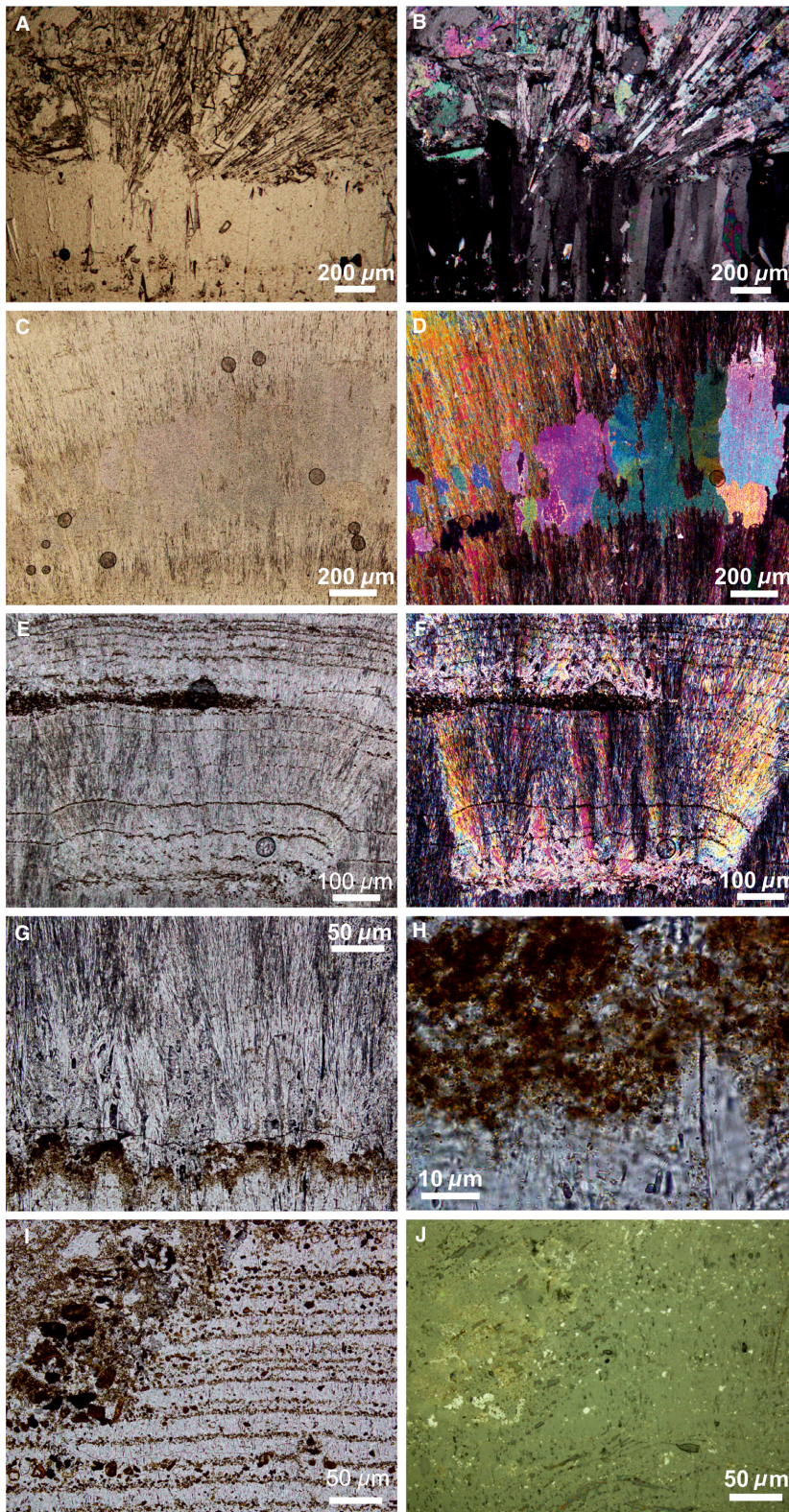


Fig. 3. Transmitted light (TL) and reflected light (RL) microscopic characterization of lamination and fabrics in erzbergite samples. (A) Radiating, fascicular aragonite layer on columnar, competitive calcite hosting linear pores (TL). (B) Cross-polarized light image of the same aragonite–calcite layers. (C) Section showing diagenetic calcite patches replacing former aragonite bundles (TL). (D) Same section affected by aragonite to calcite replacement under cross-polarized light. (E) Plane polarized and (F) cross-polarized light photomicrographs showing multiple stained particle layers within erzbergite aragonite. Note the variable thickness and intra-crystalline occurrence of these detrital layers. (G) Prominent stained particle layer of variable thickness covering former crystal terminations and providing the substrate of further competitive aragonite precipitation (TL). (H) Close-up of the selected stained particle layer highlighting the granular detrital nature (TL). (I) Transmitted light and (J) reflected light images displaying variable grain sizes and supporting a detrital origin of the coloured mineral layers. In most erzbergite samples the spatiotemporal recurrence intervals of these layers appear more variable.

Chemical characterization

Investigation of the carbonate veins included electron microprobe (EPMA) major/minor elemental mapping and back-scattered electron (BSE) imaging (Fig. 4). Analysis of sample EB3 (Fig. 4; upper maps) showed a finely laminated sequence, as well as an area of increased particle occurrence. The latter revealed highly variable grain sizes and pronounced variations in the elemental concentrations. From erzbergite sample EB2 (Fig. 4; lower maps) two prominent brownish stained layers were investigated in more detail. The overall thicker layer (darker brownish in transmitted light) is characterized by higher iron concentrations compared to the thinner layer nearby (Fig. 4; lower maps). The two stained layers are separated by a narrow zone of whitish calcium carbonate (based on Ca content and colour in transmitted light). Regarding Mg distribution the two stained layers and intercalated carbonate zone display significantly increased Mg contents. The brownish stained layers feature elevated Fe, Si and Al contents reflecting the Fe-rich (goethite) and siliceous minerals (quartz and muscovite) detected by XRD. Iron was not detected in the CaCO₃ minerals. Silicon and Al are highest in individual particles of variable size and often arranged in visually stained layers that are interlayered with the whitish aragonite–calcite successions. In addition, WDX spot analyses of selected calcites ($n = 4$) in sample EB9 yielded Mg concentrations of 3 mol % MgCO₃ in these Mg-calcites. The incorporation of Mg in the calcite crystal lattice was further evaluated by the peak position (d-spacing in Å) of the indicative [10(-1)4] peak in measured XRD spectra, i.e. an increased incorporation of relatively small Mg²⁺ ions results in shortened lattice constants (e.g. Goldsmith *et al.*, 1961; Baldermann *et al.*, 2015). Two analyses of the indicative calcite peak of erzbergite sample EB9 (XRD4 and XRD5 in Table S1) yielded 2.4 and 3.8 (±1) mol % MgCO₃ in the Mg-calcite, and the selected samples EB13 (XRD1) and EB22 (XRD2) both revealed 6.5 (±1) mol % MgCO₃ in the distinct high Mg-calcite.

Radiometric dating

In order to constrain the absolute timing and apparent rates of carbonate precipitation in fractures, 16 erzbergite samples were selected (Table 1). Most samples represent complete fracture filling indicated by remnants of adjacent fracture wall host rocks. In some cases, only two

uranium–thorium ages from subsamples as close as possible to the respective erzbergite sample ends (approximating growth inception and cessation of unidirectional samples) were measured. The particular subsample position also depended on the anticipated degree of detrital contamination (colouring) or potential diagenetic alteration, i.e. the vast majority of the selected subsamples consist of snow white aragonite. For several of the erzbergite samples multiple U–Th age measurements were conducted (Table 1) in order to evaluate their growth dynamics (for example, samples EB1 and EB2). The selection also reflects some ascribed sample relevance (first base/top ages and petrographic features), as well as overall sample thickness (thicker samples). The mass spectrometric data presented in Table 1 yielded ²³⁸U concentrations from 7 to 3120 ppb (mean 326 ppb), i.e. a broad range of very low to high (ppm level) uranium content. Similarly, the measured ²³²Th concentrations range from 20 to 96 180 ppt and consequently a large range of ²³⁰Th/²³²Th atomic ratios from 6 to 52 201 ($\times 10^{-6}$) is observed (Shen *et al.*, 2012). The absolute radiometric ages were calculated based on the most updated decay constants (Cheng *et al.*, 2013) and corrected for excess ²³⁰Th.

The ages of erzbergite precipitates range from 285.1 ± 3.9 to 1.03 ± 0.04 kyr BP (thousands of years before present = 1950 AD; Table 1) and the relative age uncertainties (2σ) in most cases amount to 0.5 to 1.0%. Some samples affected by either detrital contamination or very low U concentrations show significantly larger errors (tens of percent). For these geochemically unfavourable samples the correction procedure applied had a major effect on the final calculated age. Typical absolute age uncertainties, however, range within ± few hundreds of years, i.e. U–Th ages of high precision. For example, the youngest vein sample (sample EB7; *ca* 4 cm thick) composed exclusively of aragonite was collected on-site from a filled fracture extending tens of metres. Four measurements of selected subsamples yielded low U contents from 56 to 127 ppb but also low detrital Th contributions (Table 1). This resulted in absolute ages of 10.41 ± 0.17 (sample base and growth inception) to 1.03 ± 0.04 kyr BP (top, fracture filled) and small relative errors of 1.0 to 4.2% in spite of the very young sample age (little radiogenic ²³⁰Th ingrowth). The oldest sample (sample EB2; *ca* 10 cm thick) was provided from a collection and 17 individual U–Th ages were measured. Low to

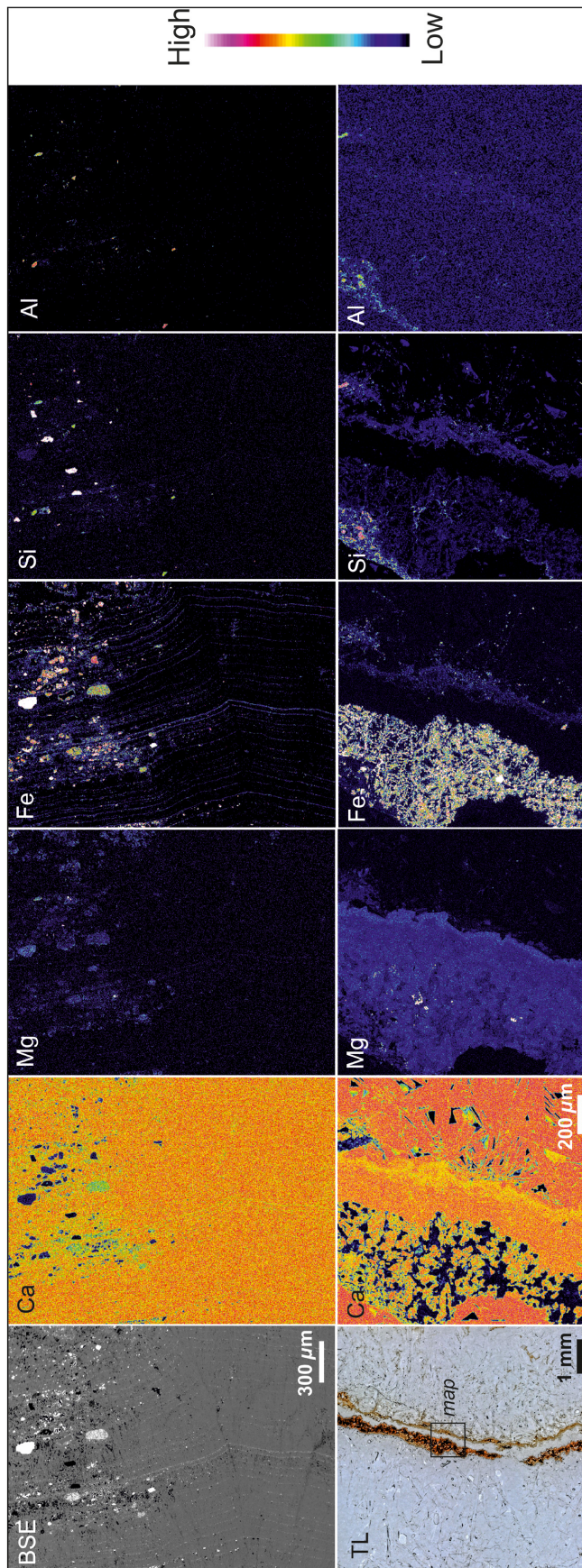


Fig. 4. Electron microprobe major and minor element concentration distributions (semi-quantitative colour code) from selected sections of the two erzbergite samples EB3 (upper maps) and EB2 (lower maps). Increased Fe, Si and Al contents are indicative of variably sized grains typically accumulated in stained particle layers. Magnesium is significantly increased in (Mg-) calcite between two prominent brownish stained layers, as well as in some of the detrital particles. High Ca concentrations characterize the dominant CaCO₃ (mostly aragonite) precipitates. Note the vertical (original) orientation of the erzbergite veins.

Table 1. ^{238}U – ^{234}U – ^{230}Th isotopic compositions and radiometric age data of erzbergite carbonate precipitates. See text for detailed explanations.

Sample*	^{238}U [ng g ⁻¹]	^{232}Th [pg g ⁻¹]	$^{230}\text{Th}/^{232}\text{Th}$ atomic $\times 10^{-6}$	$\delta^{234}\text{U}^\dagger$ measured	$^{230}\text{Th}/^{238}\text{U}$ activity	Uncorr. Age [yr]	Corr. Age [yr]	$\delta^{234}\text{U}_{\text{initial}}^\ddagger$ corr.	Age§ [yr BP]
EB1-11	68 ± 0.5	8347 ± 167	109 ± 2	500 ± 2	0.8045 ± 0.0022	79 597 ± 335	77 387 ± 1599	622 ± 4	77 322 ± 1599
EB1-41-A	330 ± 0.8	1147 ± 24	3841 ± 80	387 ± 2	0.8089 ± 0.0025	90 589 ± 450	90 521 ± 492	500 ± 3	90 456 ± 492
EB1-41-B	260 ± 0.6	687 ± 16	5081 ± 116	382 ± 2	0.8140 ± 0.0030	91 972 ± 559	91 920 ± 560	496 ± 3	91 855 ± 560
EB1-86	91 ± 0.5	281 ± 6	4449 ± 96	398 ± 2	0.8299 ± 0.0024	92 969 ± 451	92 910 ± 453	517 ± 2	92 845 ± 453
EB1-111	108 ± 0.5	3124 ± 63	598 ± 12	687 ± 2	1.0513 ± 0.0034	97 801 ± 535	97 357 ± 618	904 ± 4	97 292 ± 618
EB1-136-A	134 ± 0.2	2774 ± 56	819 ± 17	597 ± 3	1.0258 ± 0.0029	103 125 ± 531	102 790 ± 580	798 ± 4	102 725 ± 580
EB1-136-B	95 ± 0.1	1894 ± 39	842 ± 17	599 ± 2	1.0215 ± 0.0034	102 202 ± 584	101 878 ± 625	799 ± 4	101 813 ± 625
EB2-2	150 ± 0.5	288 ± 6	4047 ± 85	168 ± 2	0.4718 ± 0.0016	55 653 ± 273	55 606 ± 274	196 ± 2	55 541 ± 274
EB2-8-A	102 ± 0.2	20 ± 6	52 201 ± 14 919	142 ± 2	0.6171 ± 0.0023	83 092 ± 510	83 087 ± 510	179 ± 2	83 022 ± 510
EB2-8-B	94 ± 0.2	221 ± 9	4342 ± 170	146 ± 2	0.6221 ± 0.0026	83 589 ± 575	83 530 ± 576	184 ± 3	83 465 ± 576
EB2-14	111 ± 0.2	13 407 ± 269	94 ± 2	201 ± 2	0.6853 ± 0.0017	89 400 ± 424	86 577 ± 2040	257 ± 3	86 511 ± 2040
EB2-30	207 ± 0.4	65 ± 3	35 763 ± 1883	180 ± 2	0.6840 ± 0.0020	91 823 ± 540	91 815 ± 540	234 ± 2	91 750 ± 540
EB2-40-A	127 ± 0.2	934 ± 19	1533 ± 32	156 ± 2	0.6850 ± 0.0020	95 412 ± 567	95 234 ± 579	204 ± 2	95 169 ± 579
EB2-40-B	133 ± 0.2	939 ± 19	1600 ± 33	155 ± 2	0.6850 ± 0.0020	95 331 ± 539	95 161 ± 551	203 ± 2	95 096 ± 551
EB2-44	42 ± 0.1	480 ± 10	987 ± 21	145 ± 2	0.6787 ± 0.0021	95 138 ± 562	94 861 ± 593	189 ± 3	94 795 ± 593
EB2-50	109 ± 0.5	89 ± 2	14 043 ± 370	131 ± 2	0.6998 ± 0.0023	102 474 ± 625	102 453 ± 625	175 ± 3	102 388 ± 625
EB2-56	62 ± 0.1	69 ± 2	10 609 ± 368	146 ± 2	0.7193 ± 0.0018	104 681 ± 551	104 654 ± 551	196 ± 3	104 588 ± 551
EB2-63	55 ± 0.1	269 ± 6	2732 ± 64	217 ± 2	0.8163 ± 0.0025	115 617 ± 716	115 506 ± 719	300 ± 3	115 440 ± 719
EB2-70-A	56 ± 0.1	289 ± 7	2718 ± 65	220 ± 2	0.8513 ± 0.0033	123 642 ± 911	123 527 ± 913	312 ± 2	123 462 ± 913
EB2-70-B	50 ± 0.1	245 ± 8	2906 ± 94	229 ± 2	0.8698 ± 0.0034	126 689 ± 1027	126 580 ± 1029	327 ± 3	126 515 ± 1029
EB2-80	97 ± 0.2	775 ± 16	1694 ± 35	165 ± 2	0.8218 ± 0.0020	127 484 ± 745	127 295 ± 755	237 ± 3	127 229 ± 755
EB2-84	151 ± 0.2	2102 ± 42	970 ± 20	158 ± 2	0.8194 ± 0.0017	128 555 ± 620	128 224 ± 661	226 ± 2	128 158 ± 661
EB2-89	122 ± 0.5	2218 ± 45	1020 ± 21	164 ± 2	1.1258 ± 0.0029	285 571 ± 3903	285 182 ± 3899	368 ± 6	285 117 ± 3899
EB2-95	105 ± 0.1	850 ± 18	2128 ± 44	155 ± 2	1.0500 ± 0.0023	229 879 ± 2144	229 695 ± 2144	296 ± 4	229 629 ± 2144
EB3-2	265 ± 1.0	29 992 ± 607	22 ± 1	321 ± 2	0.1540 ± 0.0007	13 449 ± 66	10 949 ± 1772	331 ± 3	10 884 ± 1772
EB3-26-A	136 ± 0.5	85 914 ± 1728	6 ± 1	304 ± 2	0.2397 ± 0.0012	21 975 ± 129	7018 ± 10 720	310 ± 10	6953 ± 10 720
EB3-26-B	149 ± 0.5	96 180 ± 1936	6 ± 1	302 ± 2	0.2389 ± 0.0013	21 924 ± 133	6588 ± 10 998	308 ± 10	6523 ± 10 998
EB3-46-A	26 ± 0.04	757 ± 16	82 ± 3	298 ± 3	0.1462 ± 0.0032	12 972 ± 305	12 316 ± 554	309 ± 3	12 251 ± 554
EB3-46-B	39 ± 0.1	1344 ± 28	76 ± 2	309 ± 3	0.1594 ± 0.0020	14 089 ± 190	13 323 ± 574	321 ± 3	13 258 ± 574
EB3-46-C	45 ± 0.1	1375 ± 29	78 ± 2	303 ± 3	0.1447 ± 0.0027	12 786 ± 254	12 105 ± 544	313 ± 3	12 040 ± 544
EB5-6-A	130 ± 0.5	4953 ± 100	318 ± 6	23.9 ± 1.6	0.7340 ± 0.0021	136 499 ± 920	135 422 ± 1185	35 ± 2	135 357 ± 1185
EB5-6-B	109 ± 0.5	4123 ± 83	317 ± 6	24.9 ± 1.4	0.7282 ± 0.0019	133 367 ± 790	132 300 ± 1086	36 ± 2	132 235 ± 1086
EB5-100	79 ± 0.2	9998 ± 201	98 ± 2	47.0 ± 2.0	0.7540 ± 0.0020	136 544 ± 1018	133 037 ± 2668	69 ± 3	132 972 ± 2668
EB5-130-A	75 ± 0.1	7582 ± 152	108 ± 2	13.0 ± 2.0	0.6630 ± 0.0020	115 485 ± 854	112 560 ± 2228	18 ± 2	112 495 ± 2228
EB5-130-B	75 ± 0.2	7910 ± 159	103 ± 2	8.0 ± 2.0	0.6560 ± 0.0030	114 622 ± 970	111 540 ± 2373	11 ± 3	111 475 ± 2373
EB5-158	56 ± 0.1	1228 ± 25	476 ± 10	28.0 ± 2.0	0.6380 ± 0.0030	105 040 ± 820	104 419 ± 925	37 ± 3	104 354 ± 925
EB5-195-A	42 ± 0.5	353 ± 7	1204 ± 25	34.9 ± 1.6	0.6098 ± 0.0017	96 364 ± 493	96 132 ± 519	46 ± 2	96 067 ± 519
EB5-195-B	41 ± 0.5	344 ± 7	1207 ± 25	33.8 ± 1.6	0.6143 ± 0.0020	97 679 ± 570	97 445 ± 592	44 ± 2	97 380 ± 592
EB6-10	67 ± 0.1	24 ± 1	3660 ± 185	145 ± 2	0.0803 ± 0.0004	7920 ± 47	7911 ± 48	148 ± 2	7845 ± 48
EB6-20	124 ± 0.2	671 ± 16	399 ± 10	144 ± 2	0.1320 ± 0.0010	13 284 ± 130	13 147 ± 162	149 ± 2	13 082 ± 162
EB6-90	548 ± 1.5	9606 ± 194	139 ± 3	134 ± 2	0.1480 ± 0.0010	15 173 ± 86	14 724 ± 329	139 ± 2	14 659 ± 329
EB7-1	127 ± 0.3	260 ± 6	101 ± 3	195 ± 2	0.0125 ± 0.0003	1140 ± 25	1091 ± 43	206 ± 2	1025 ± 43
EB7-7-A	56 ± 0.1	43 ± 4	832 ± 87	199 ± 2	0.0390 ± 0.0010	3610 ± 98	3591 ± 99	201 ± 2	3526 ± 99
EB7-7-B	56 ± 0.1	43 ± 1	726 ± 21	198 ± 2	0.0340 ± 0.0005	3106 ± 29	3087 ± 31	200 ± 2	3022 ± 31

Table 1. (continued)

Sample*	^{238}U [ng g ⁻¹]	^{232}Th [pg g ⁻¹]	$^{230}\text{Th}/^{232}\text{Th}$ atomic $\times 10^{-6}$	$\delta^{234}\text{U}^\dagger$ measured	$^{230}\text{Th}/^{238}\text{U}$ activity	Uncorr. Age [yr]	Corr. Age [yr]	$\delta^{234}\text{U}_{\text{initial}}^\ddagger$ corr.	Age§ [yr BP]
EB7-33	122 ± 0.2	853 ± 20	270 ± 7	231 ± 2	0.1150 ± 0.0010	10 637 ± 125	10 473 ± 171	238 ± 2	10 408 ± 171
EB12-9	59 ± 0.1	4856 ± 98	13 ± 1	120 ± 3	0.0650 ± 0.0030	6533 ± 262	4361 ± 1559	121 ± 3	4296 ± 1559
EB12-12	190 ± 0.4	2473 ± 50	68 ± 1	121 ± 2	0.0542 ± 0.0003	5398 ± 30	5059 ± 241	122 ± 2	4993 ± 241
EB12-22A	139 ± 0.2	949 ± 22	334 ± 8	114 ± 2	0.1380 ± 0.0010	14 411 ± 141	14 234 ± 189	118 ± 2	14 169 ± 189
EB13-27	309 ± 0.7	3643 ± 74	1157 ± 24	280 ± 3	0.8280 ± 0.0030	107 653 ± 762	107 403 ± 780	379 ± 4	107 338 ± 780
EB13-125	862 ± 2	11 466 ± 231	996 ± 20	195 ± 2	0.8030 ± 0.0020	116 409 ± 687	116 104 ± 718	270 ± 3	116 039 ± 718
EB14-4	1316 ± 2	1377 ± 30	11 783 ± 256	202 ± 2	0.7478 ± 0.0017	102 210 ± 490	102 185 ± 490	270 ± 3	102 119 ± 490
EB14-197	3120 ± 5	4709 ± 95	8478 ± 172	162 ± 2	0.7761 ± 0.0017	115 864 ± 589	115 828 ± 589	224 ± 3	115 762 ± 589
EB15-5	103 ± 0.2	706 ± 18	3089 ± 79	443 ± 3	1.2880 ± 0.0080	195 586 ± 3248	195 473 ± 3246	769 ± 8	195 408 ± 3246
EB15-100	90 ± 0.2	16 047 ± 323	115 ± 2	328 ± 2	1.2480 ± 0.0070	232 957 ± 4380	229 720 ± 4841	628 ± 10	229 655 ± 4841
EB15-110	57 ± 0.1	58 060 ± 1166	18 ± 0.4	210 ± 2	1.1355 ± 0.0034	246 218 ± 2984	222 720 ± 17 302	394 ± 20	222 654 ± 17 302
EB16-2-A	212 ± 0.3	1049 ± 22	1504 ± 31	363 ± 2	0.4516 ± 0.0012	43 070 ± 161	42 967 ± 176	409 ± 2	42 901 ± 176
EB16-2-B	251 ± 0.3	1148 ± 24	1626 ± 34	363 ± 2	0.4507 ± 0.0014	42 969 ± 183	42 875 ± 195	409 ± 3	42 809 ± 195
EB16-42	1024 ± 3.6	158 ± 13	49 996 ± 4061	380 ± 3	0.4680 ± 0.0030	44 298 ± 320	44 295 ± 320	431 ± 3	44 230 ± 320
EB17-11	447 ± 1.3	5036 ± 102	122 ± 3	33.0 ± 2.0	0.0830 ± 0.0010	9166 ± 63	8849 ± 233	34 ± 2	8784 ± 233
EB17-78	321 ± 1.0	19 167 ± 388	29 ± 1	13.0 ± 2.0	0.1060 ± 0.0010	12 043 ± 92	10 312 ± 1227	14 ± 2	10 247 ± 1227
EB17-83	801 ± 2	1160 ± 24	1160 ± 24	31.5 ± 1.9	0.1019 ± 0.0004	11 341 ± 49	11 300 ± 57	33 ± 2	11 234 ± 57
EB18-6	61 ± 0.2	9671 ± 196	11 ± 1	280 ± 4	0.1050 ± 0.0020	9342 ± 206	5721 ± 2573	285 ± 5	5656 ± 2573
EB19-4	7 ± 0.5	1218 ± 26	8 ± 1	142 ± 6	0.0800 ± 0.0140	7935 ± 1393	3518 ± 3404	144 ± 6	3453 ± 3404
EB19-29	7 ± 0.01	1929 ± 39	12 ± 0.3	165 ± 3	0.1898 ± 0.0026	19 312 ± 293	12 511 ± 4833	171 ± 3	12 445 ± 4833
EB19-117	108 ± 0.3	3499 ± 71	52 ± 1	127 ± 3	0.1020 ± 0.0020	10 343 ± 163	9509 ± 611	130 ± 3	9444 ± 611
EB21-2	119 ± 0.2	285 ± 6	232 ± 5	92.3 ± 1.6	0.0336 ± 0.0003	3402 ± 28	3338 ± 53	93 ± 2	3272 ± 53
EB21-25	313 ± 1	1430 ± 29	335 ± 7	93.8 ± 1.8	0.0929 ± 0.0003	9669 ± 38	9548 ± 94	96 ± 2	9482 ± 94
EB21-55	366 ± 0.9	31 095 ± 628	24 ± 1	99.4 ± 1.9	0.1257 ± 0.0006	13 214 ± 66	10 951 ± 1602	103 ± 2	10 885 ± 1602
EB23-16-A	2587 ± 5	14 717 ± 296	126 ± 3	21.8 ± 1.9	0.0436 ± 0.0002	4752 ± 22	4590 ± 117	22 ± 2	4524 ± 117
EB23-16-B	2367 ± 19.2	4503 ± 98	387 ± 9	15.8 ± 3.3	0.0446 ± 0.0004	4896 ± 48	4841 ± 61	16 ± 3	4775 ± 61
EB23-27	2720 ± 8	14 026 ± 284	206 ± 4	9.6 ± 1.8	0.0644 ± 0.0003	7182 ± 32	7033 ± 110	10 ± 2	6967 ± 110

Uncertainties reported as 2σ . U decay constants: $\lambda_{238} = 1.55125 \times 10^{-10}$ (Jaffey et al., 1971) and $\lambda_{234} = 2.82206 \times 10^{-6}$ (Cheng et al., 2013). Th decay constant: $\lambda_{230} = 9.1705 \times 10^{-6}$ (Cheng et al., 2013).

*Second number typically denotes the distance from a fracture wall (base/top) in mm; A, B denote replicate measurements.

† $\delta^{234}\text{U} = \left(\frac{^{234}\text{U}/^{238}\text{U}}{\text{activity} - 1} \right) \times 1000$. $\delta^{234}\text{U}_{\text{initial}}$ calculated based on ^{230}Th age (T), i.e., $\delta^{234}\text{U}_{\text{initial}} = \delta^{234}\text{U}_{\text{measured}} \times e^{2.34 \times T}$.

‡Corrected ^{230}Th ages assume the initial $^{230}\text{Th}/^{232}\text{Th}$ atomic ratio of $4.4 \pm 2.2 \times 10^{-6}$. Those are the values for a material at secular equilibrium, with the bulk earth $^{230}\text{Th}/^{238}\text{U}$ value of 3.8 and errors are arbitrarily assumed to be 50%.

§Corrected and referenced; yr BP stands for 'years Before Present' where the present is defined as the year 1950 AD.

intermediate U contents range from 42 to 207 ppb and detrital Th contamination (based on ^{232}Th value) is typically low. This prominent aragonite–calcite sample comprises absolute ages from 285.1 ± 3.9 to 55.54 ± 0.27 kyr BP (Table 1) with small relative errors of 0.5 to 2.4% (mostly 0.6%). It represents a rare erzbergite sample possessing a large depositional time range. Several growth interruptions, however, are documented based on the U–Th dating results and also the petrography. With regard to typical (average) erzbergite precipitation (growth) rates some approximations can be inferred from the U–Th age distributions of selected precisely dated subsamples based on measured age differences. The inferred growth rates range between *ca* 0.003 and 0.029 mm year $^{-1}$ (Table S2) and are typically in the range of a few tens of micrometres per year.

Carbonate stable carbon, oxygen and clumped isotopes

Stable C and O isotopes

Overall stable isotope values measured from aragonite and calcite of erzbergite precipitates revealed a wide range from -0.7 to $+6.8\text{‰}$ (VPDB) and -11.5 to -5.1‰ (VPDB) for $\delta^{13}\text{C}$ and $\delta^{18}\text{O}$, respectively (Table S3; Fig. 5). Sample EB22 shows prominently low $\delta^{13}\text{C}$ values from -0.7 to 0.2‰ (mean: -0.3‰) but high $\delta^{18}\text{O}$ values of -8.2 to -6.4‰ (mean: -7.5‰). Several erzbergite samples (EB1, EB6, EB12, EB17, EB23 and EB24) display some tendency of concurrently high $\delta^{13}\text{C}$ and $\delta^{18}\text{O}$ (Fig. 5). In the case of erzbergite sample EB2, a continuous and higher spatial resolution (1 mm) stable isotope transect was analyzed (Table S4). The measured $\delta^{13}\text{C}$ values vary from 1.1 to 5.3‰ (VPDB; mean: 3.2‰) and the $\delta^{18}\text{O}$ values range from -11.5 to -7.3‰ (VPDB; mean: -8.8‰).

Stable C and O isotopic compositions were further analyzed from different host rock carbonates. Siderite (iron ore) subsamples (SID in Table S3; Fig. 5) revealed prominently low C as well as O isotope values from -7.7 to -4.3‰ (VPDB; mean: -6.1‰) and -14.5 to -13.3‰ (VPDB; mean: -13.6‰), respectively. In contrast, the ankerite samples show higher $\delta^{13}\text{C}$ of -4.0 to -0.5‰ (mean: -1.4) and also higher $\delta^{18}\text{O}$ of -13.8 to -10.8‰ (mean: -12.2‰ ; ANK in Table S3; Fig. 5). However, these values are still low compared to the erzbergite $\delta^{13}\text{C}$ and $\delta^{18}\text{O}$ compositions. Isotope analyses of the local limestone (Sauberger Kalk; SK in Table S3; Fig. 5) yielded $\delta^{13}\text{C}$ values from 0.7 to 1.3‰ (mean: 1.0) and $\delta^{18}\text{O}$ values from -9.0 to -7.9‰ (mean: -8.4), i.e.

significantly higher in relation to the other host rock (iron) carbonates. The local limestone C and O isotope compositions are thus comparable to the erzbergite precipitates of low $\delta^{13}\text{C}$ and intermediate (typical) $\delta^{18}\text{O}$ (Fig. 5). The new iron ore C and O isotope data presented agree well with siderite and ankerite isotope ranges (black rectangles in Fig. 5) reported in Weber (1997). The limestone compositions (SK), however, revealed somewhat higher $\delta^{18}\text{O}$ values compared with earlier work (blue rectangles in Fig. 5; Weber, 1997).

Clumped isotopes

Carbonate clumped isotope (multiply-substituted isotopologue) measurements were conducted on five different erzbergite fracture fillings from Erzberg (Table 2). From two of the selected samples, two distinct subsamples were analyzed (samples EB1 and EB12) and the unaltered mineralogy

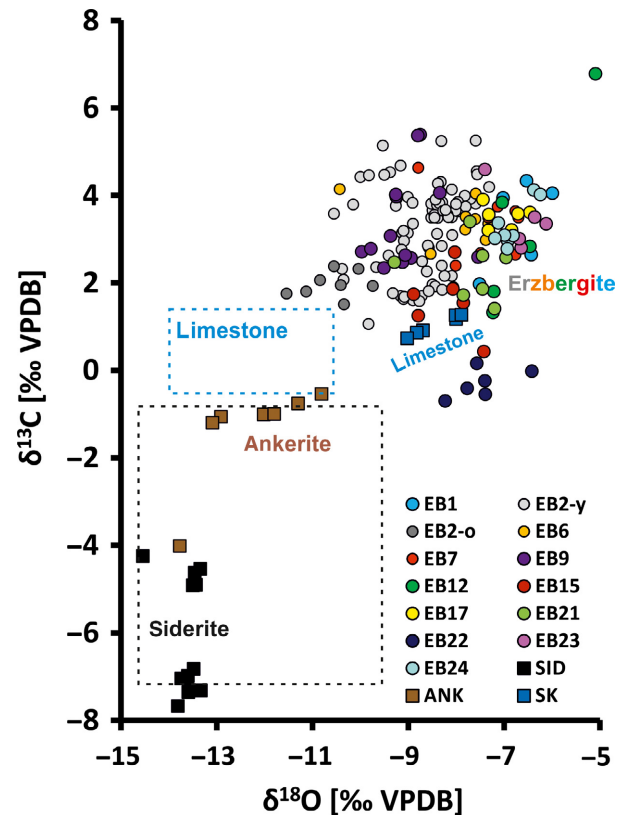


Fig. 5. Stable O versus C isotopic composition of erzbergite (aragonite–calcite) precipitates, as well as of local host rock carbonates (SID: siderite, ANK: ankerite, SK: limestone calcite). The dashed rectangles mark isotope ranges for siderite/ankerite (black) and limestone (blue) reported in Weber (1997). Note the high variability of the EB precipitates and major differences between the different host rock (iron ore) carbonates.

(aragonite) was confirmed by XRD before isotope measurement. The Δ_{47} values measured range from 0.744 to 0.767‰ (mean: 0.758‰) which corresponds to temperatures of around +2 to +9°C (mean: ca 5°C) when applying the temperature calibration of Kluge *et al.* (2015). The measured replicates ($n = 3$ to 4) result in Δ_{47} uncertainties of around ± 0.015 ‰ and consequently in temperature uncertainties of ± 2 to 8°C. Essentially, these first determinations suggest low ambient formation (water) temperatures of <10 °C for the vein precipitates. Regarding CaCO₃ precipitation from low saline aqueous solution, 0°C (freezing conditions) have to be considered as a lower limit of erzbergite formation. The subsamples of EB1 and EB12 yielded similar temperatures within uncertainties (Table 2). Apart from the clumped isotopic composition the calcium carbonate mass spectrometric analysis also provided the corresponding stable C and O isotopic compositions (Table 2). The $\delta^{13}\text{C}$ values range from +2.2 to +5.6‰ (VPDB; mean: 3.4‰) and $\delta^{18}\text{O}$ values vary from -8.8 to -7.0‰ (VPDB; mean: -8.1‰). These values are very similar to those obtained from the erzbergite stable isotope analyses based on conventional continuous-flow isotope ratio mass spectrometry (CF-IR-MS; Table S3; Fig. 5). Aqueous solution (palaeofluid) $\delta^{18}\text{O}$ values inferred from the carbonate clumped isotope measurements range from -11.8 to -8.7‰ (VSMOW; mean: -10.8‰; Table 2).

Modern hydrochemistry

Water chemistry and stable isotopic compositions were measured from modern fracture and surface waters. The typically small water flows (less than a litre per second) were encountered at different levels of the mine, i.e. altitudes between 700 m and 950 m above sea-level (m a.s.l.) (Fig. 1). The sampling sites are scattered across the open pit mine but can be ordered into southern, central and northern sections (Fig. 1). Aqueous solution electric conductivities (EC) measured in the field ranged between 488 $\mu\text{S cm}^{-1}$ and 1456 $\mu\text{S cm}^{-1}$ reflecting the overall high total dissolved solid (TDS) contents of up to 1273 mg l⁻¹ determined in the laboratory (Table 3). The corresponding pH values showed a narrow range of 8.1 to 8.8 and water temperatures measured on-site at the surface varied significantly from 8.8 to 25.3°C.

Regarding the dominant cations in aqueous solution, the Na and K concentrations yielded variable values from 1.2 to 19 mg l⁻¹ and 0.9 to

Table 2. Overview of aragonite (erzbergite) clumped isotope (multiply-substituted isotopologue) measurements conducted at Erzberg. The analyses revealed overall low aragonite formation (water) temperatures of CaCO₃ precipitation in vertical fractures.

Sample	Mineralogy (XRD)	$\delta^{13}\text{C}$ ‰ VPDB	$\delta^{18}\text{O}$ ‰ VPDB	Δ_{47} meas. ‰	Replicates (n)	T from Δ_{47} * °C	$\delta^{18}\text{O}$ _water ‰ VSMOW
EB1-CI1	Aragonite	2.36 ± 0.19	-8.23 ± 0.23	0.761 ± 0.016	3	4 ± 3	-11.1 ± 1.0
EB1-CI2	Aragonite	2.93 ± 0.29	-7.99 ± 0.67	0.767 ± 0.024	3	2 ± 8	-11.3 ± 2.1
EB6-CI1	Aragonite	3.78 ± 0.28	-8.65 ± 0.24	0.765 ± 0.017	4	3 ± 5	-11.8 ± 1.5
EB7-CI1	Aragonite	3.46 ± 0.18	-8.13 ± 0.39	0.764 ± 0.021	3	3 ± 7	-11.3 ± 1.8
EB12-CI1	Aragonite	5.58 ± 0.12	-7.85 ± 0.23	0.749 ± 0.005	3	8 ± 2	-9.8 ± 0.9
EB12-CI2	Aragonite	3.66 ± 0.40	-6.95 ± 0.26	0.744 ± 0.012	3	9 ± 4	-8.7 ± 1.2
EB21-CI1	Aragonite	2.21 ± 0.29	-8.78 ± 0.07	0.757 ± 0.012	3	5 ± 4	-11.4 ± 1.2

*Using Kluge *et al.* (2015), 0.269 as intercept. Uncertainties: SD for $\delta^{13}\text{C}$ and $\delta^{18}\text{O}$, SE for Δ_{47} and T. Uncertainty of $\delta^{18}\text{O}$ _water includes T uncertainty, uncertainty in carbonate $\delta^{18}\text{O}$ and uncertainty in alpha(aragonite-H₂O).

Table 3. Hydrochemical and stable isotopic compositions of modern water samples collected at Erzberg. The data include field-based parameters, major, minor and trace constituents in aqueous solution, stable isotopes of the water and dissolved species, as well as calculated aragonite, calcite and CO₂ saturation states. Note the highly variable but indicative (water type) compositions and high CaCO₃ supersaturation.

Sample ID	Location Level, Section of Erzberg	Elevation [m]	Water-T [°C]	EC [µS cm ⁻¹]	pH	Na ⁺ K ⁺ Mg ²⁺ Ca ²⁺ F ⁻ Cl ⁻ NO ₃ ⁻ HCO ₃ ⁻ SO ₄ ²⁻ SO ₄ ²⁻ Al Ba Cr Fe Li Mn Si Sr Zn δ ² H δ ¹⁸ O										D-excess [‰]	δ ¹³ C _{DIC} [‰ VPDB]	δ ³⁴ S _{SO4} [‰ VCDT]	SL_Arag log	SL_Cc log	P _{CO2} log										
						Na ⁺ [mg l ⁻¹]	K ⁺ [mg l ⁻¹]	Mg ²⁺ [mg l ⁻¹]	Ca ²⁺ [mg l ⁻¹]	F ⁻ [mg l ⁻¹]	Cl ⁻ [mg l ⁻¹]	NO ₃ ⁻ [mg l ⁻¹]	HCO ₃ ⁻ [mg l ⁻¹]	SO ₄ ²⁻ [mg l ⁻¹]	SO ₄ ²⁻ [mg l ⁻¹]							Al [µg l ⁻¹]	Ba [µg l ⁻¹]	Cr [µg l ⁻¹]	Fe [µg l ⁻¹]	Li [µg l ⁻¹]	Mn [µg l ⁻¹]	Si [µg l ⁻¹]	Sr [µg l ⁻¹]	Zn [µg l ⁻¹]	δ ² H [‰ VSMOW]
WEB1	16-Jul-15	Antoni, South	25.3	960	8.75	2.6	2.4	145	9.3	n.a.	3.5	2.3	685	63	18	1	4	4	14	8	1	4	2	-64.4	-8.8	1.6	n.a.	n.a.	0.8	0.9	-3.0
WEB2	16-Jul-15	Engstelle 242, North	14.1	488	8.40	1.2	0.9	42	43	<0.1	1.0	3.6	326	17	45	89	<1	6	7	<1	3	218	1	-78.7	-11.1	4.6	n.a.	n.a.	0.7	0.9	-3.0
WEB3	16-Jul-15	Oberegger, South	24.9	807	8.79	1.9	3.9	115	12	<0.1	3.2	1.0	546	58	18	31	3	9	14	<1	1	46	1	-55.2	-7.7	2.8	n.a.	n.a.	0.8	0.9	-3.2
WEB4	16-Jul-15	Oberegger, South	23.9	959	8.38	1.2	1.7	105	67	<0.1	2.1	2.0	716	20	51	1	2	2	11	<1	1	28	1	-54.3	-8.0	5.7	n.a.	n.a.	1.3	1.4	-2.6
WEB5	16-Jul-15	Sybold, Center	15.0	1344	8.15	12	5.0	132	91	n.a.	20	13	694	186	63	50	3	4	57	<1	1	111	2	-65.8	-9.6	6.0	n.a.	n.a.	1.1	1.2	-2.4
WEB5-2	22-Apr-16	Sybold, Center	8.8	1456	8.20	15	5.0	153	91	<0.1	26	2.4	747	226	58	41	<1	78	80	23	1	113	2	-78.4	-11.1	4.8	3.0	-2.8	1.0	1.2	-2.5
WEB6	22-Apr-16	ETM5, Center	15.3	1312	8.18	18	5.2	123	96	<0.1	37	8.4	602	220	57	23	<1	2	95	53	1	141	3	-76.4	-10.8	4.4	2.4	2.5	1.0	1.2	-2.5
WEB7	22-Apr-16	Palmer, South	12.8	964	8.76	3.6	9.3	140	14	<0.1	9.6	0.6	636	81	15	12	2	9	18	<1	1	9	2	-68.1	-9.1	0.2	3.8	n.a.	0.7	0.8	-3.1
WEB8	22-Apr-16	Oberegger, Center	11.3	1420	8.06	15	5.4	146	107	<0.1	26	4.2	757	221	56	21	1	3	68	5	1	126	1	-78.1	-11.2	6.1	2.4	-4.9	1.0	1.1	-2.3
WEB9	22-Apr-16	Etage 3, South	21.9	775	8.67	3.6	2.9	111	14	<0.1	4.3	1.5	549	35	17	2	2	<1	18	2	1	5	1	-65.7	-8.6	-1.1	3.5	n.a.	0.7	0.8	-3.0

9.3 mg l⁻¹, respectively (Table 3). The Ca contents also revealed a high variability from 9.3 mg l⁻¹ up to 107 mg l⁻¹ and the overall high Mg contents varied from 42 mg l⁻¹ up to 153 mg l⁻¹. Importantly, these waters exhibit prominently high molar Mg²⁺/Ca²⁺ ratios from 2 up to 26. Considering the dominant anions, the chloride and nitrate concentrations varied from 1 to 37 mg l⁻¹ and 0.6 to 13 mg l⁻¹, respectively (Table 3). The dissolved sulphate contents are mostly elevated, displaying values from 16.7 to 226 mg l⁻¹. Similarly, the waters showed variable but generally high HCO₃⁻ concentrations from 326 to 757 mg l⁻¹. Based on the major ion compositions, the waters encountered can be classified into three different water types, i.e. Mg–HCO₃, Mg–Ca–HCO₃ and Mg–Ca–HCO₃–SO₄ waters. From the analytical results of selected trace elements, the total dissolved Fe contents are typically low (2 to 10 µg l⁻¹) with maximum concentrations of 78 µg l⁻¹. Aluminum concentrations did not exceed 63 µg l⁻¹ and the Sr values were also low ranging from 4 to 218 µg l⁻¹ (Table 3). Based on the hydrochemical analyses, the calculated CaCO₃ saturation states yielded prominently high SI values from 0.7 to 1.3 for aragonite and 0.8 to 1.4 for calcite (Table 3). In addition, the modelled carbon dioxide partial pressures of these waters resulted in log₁₀P_{CO2} (atm) values of –3.2 to –2.3, i.e. significantly elevated compared to ambient atmospheric values (*ca* –3.4).

Stable isotope analyses of the modern waters and dissolved constituents revealed variable δ²H values from –78.7 to –54.3‰ (VSMOW) and also distinct variations in δ¹⁸O ranging from –11.2 to –7.7‰ (VSMOW; Table 3). The calculated deuterium excesses of the measured δ²H versus δ¹⁸O couples vary from –1.1 to 6.1‰ (average = 3.5‰; referenced to the Austrian Meteoric Water Line; Hager & Foelsche, 2015). The δ¹³C compositions of dissolved inorganic carbon (DIC) yielded prominently high values of +2.4 to +3.8‰ (VPDB). In addition, δ³⁴S values of dissolved sulphate in selected water samples ranged from –4.9 to +2.5‰ (VCDT).

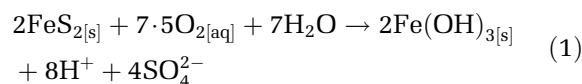
DISCUSSION

Sulphide oxidation and CaCO₃ precipitation

Sulphide oxidation

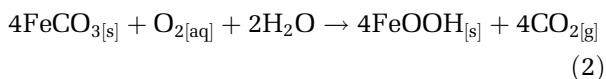
Several lines of evidence support sulphide oxidation and concomitant sulphuric acid evolution in

the aqueous solution as the principal hydrochemical mechanism of efficient host rock dissolution, mobilization and subsequent aragonite–calcite precipitation in fractures. The high δ¹³C values of the erzbergite precipitates (–0.7 to +6.8‰ VPDB; Fig. 5) evolve from the relatively high C isotopic signature of local limestone and ankerite host rocks. These values argue against a significant contribution of isotopically light CO₂ (*ca* –25 to –15‰ VPDB) and associated carbonic acid (H₂CO₃^{*}) for carbonate dissolution originating from the soil zone due to vegetation activity and microbial degradation processes above the aquifer (Deines *et al.*, 1974; Fairchild *et al.*, 2006). Modern waters collected at Erzberg also revealed conspicuously high δ¹³C values (2.4 to 3.8‰ in DIC; Table 3), as well as high sulphate concentrations (SO₄²⁻ up to 226 mg l⁻¹). Sulphide oxidation and sulphuric acid based dissolution is further corroborated by sulphur stable isotope analyses of dissolved sulphate which yielded δ³⁴S compositions of –4.9 to +2.5‰ VCDT (Table 3), i.e. values comparable to the sulphide reference standard (VCDT), as well as to scarce values of iron sulphides from Erzberg (–2.2 to +5.1‰ VCDT; Weber, 1997) and significantly different from typical seawater/evaporite signatures (around +20‰ VCDT; Mittermayr *et al.*, 2012; Hoefs, 2015). Intense water–rock interaction resulting from the action of a strong (sulphuric) acid is also reflected in the overall high ionic strength of the modern fracture and surface waters (TDS up to 1273 mg l⁻¹ and EC up to 1456 µS cm⁻¹; Table 3). Importantly, pyrite (FeS₂) and other metal (Cu, Zn and Hg) sulphides are widespread accessory minerals at Erzberg, i.e. disseminated or as veins in the iron ore carbonates (siderite and ankerite) and in dark Carboniferous schists (Schulz *et al.*, 1997). It has to be noted that the relevance of sulphide (pyrite) oxidation for carbonate dissolution and precipitation at Erzberg was already recognized by some of the early mining geologists (Angel, 1939). A more detailed process understanding of erzbergite formation, however, was not elaborated on. The oxidation (weathering) of pyrite and subsequent Fe (III)-hydroxide precipitation can be expressed by the overall chemical reaction:

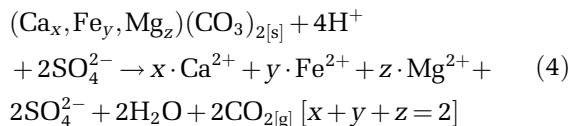
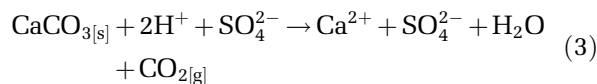


According to Eq. 1, pyrite dissolution relies on the availability of oxygen containing (oxidizing)

waters, i.e. most likely waters of meteoric origin which probably endure short residence times in the aquifer (months to a few years). The low $\delta^{18}\text{O}$ values of the erzbergite samples (-11.5 to -5.1‰ VPDB) strongly support a meteoric origin and low ambient formation (water) temperatures of these carbonate precipitates. This is further corroborated by the indicative $\delta^{18}\text{O}$ of the palaeofluid calculated from $\delta^{18}\text{O}$ of carbonate and the clumped isotope Δ_{47} temperatures measured (Table 2). Stable isotopic compositions ($\delta^{18}\text{O}$ from -11.2 to -7.7‰ VSMOW) of modern fracture and surface waters at Erzberg also show a variable but common regional meteoric signature (Table 3). Further, pyrite weathering involves the oxidation of Fe (Fe^{2+} to Fe^{3+}) typically associated with the precipitation of iron (oxy)hydroxides (for example, goethite detected by XRD). The occurrence of brownish Fe-rich layers within most of the erzbergite samples therefore partially results from the mobilization of oxidized iron minerals (goethite). A catalytical function of chemoautolithotroph microbes (iron bacteria and fungi; Pirajno, 2009, and references therein) might be involved in this redox reaction. This aspect, however, is not a focus of the current study. Also, the widespread oxidative weathering of siderite (FeCO_3) during interaction with oxygen containing waters in the fractures (vadose fissured aquifer) or at the surface is considered of major importance with regard to the formation of iron (oxy)hydroxides (Bachan & Kump, 2015). The mobilization of such Fe^{2+} -carbonate derived corrosion phases contributes to the recurrent brownish stained layers including goethite in the erzbergite. More generally, siderite and ankerite oxidation are the primary reason for the rusty look of the open pit iron ore mine (Figs 1 and 2). The latter process of variable intensity might be described by the overall reaction:



Regarding an efficient dissolution of different host rock carbonates and potential vein carbonate precipitation at Erzberg, the evolution of sulphuric acid in the local waters from sulphide (pyrite) oxidation constitutes a crucial prerequisite. The dissolution of limestone calcite or chemically more diverse ankerite by sulphuric acid can be expressed by the following principal reactions:



Source rocks

The different carbonate host rock solubilities (solubility product $\log K_{\text{SP}}$ of calcite: $ca -8.5$; dolomite: $ca -17.1/2 = -8.6$; ankerite: $ca -19.9/2 = -10.0$ depending on stoichiometry; siderite: $ca -10.9$; cf. Morse & Mackenzie, 1990) in connection with spatiotemporally variable water flow routes are probably of major relevance for carbonate mobilization and subsequent precipitation in fractures. Based on measured stable C versus O isotope distributions of the erzbergite and host rock carbonates (Fig. 5), the Devonian limestones (SK = Sauberger Kalk) are identified as an important source of calcium carbonate (Fig. 5). In some sections of the mine and associated water flows, the widespread Devonian carbonates might exhibit a more dolomitic composition (Schulz *et al.*, 1997), i.e. affecting the solubility behaviour and Mg concentrations in aqueous solution. Siderite iron ore, in contrast, shows much lower $\delta^{13}\text{C}$ and $\delta^{18}\text{O}$ values (SID in Fig. 5) compared to the precipitated CaCO_3 in fractures and is therefore not considered to be a major source here. Ankerite stable isotopic analyses yielded somewhat lower $\delta^{13}\text{C}$ and $\delta^{18}\text{O}$ values (ANK in Fig. 5) compared to the SK host rock and the values are close to some of the erzbergite samples (for example, sample EB22). The principal chemical mechanisms discussed previously are also supported by a detailed mineralogical characterization of sample EB22 (Fig. 2E), which is a host rock component of greyish colour adjacent to layered erzbergite carbonate and was shown via XRD to contain ankerite (Table S1), and microscopic inspection revealed minor occurrences of sulphides and siliceous minerals. A fine network of prominent red-brownish veins dissecting this iron ore component (Fig. 2E) was shown to contain ankerite, Mg-calcite and goethite by XRD analysis (Table S1). In essence, both the stable isotopic and mineralogical composition of this particular sample support ankerite host rock dissolution through sulphide oxidation and

sulphuric acid generation, leading to Ca (plus Mg and Fe) carbonate mobilization and concurrent Fe oxidation, and finally vein mineralization in the form of aragonite or Mg-calcite, as well as goethite in fractures of the host rock carbonate.

pH and CO₂ outgassing

Considering the variable dissolution of limestone calcite (SK) and ankerite as the identified primary carbonate sources of successive erzbergite precipitation, the interaction with sulphuric acid containing aqueous solutions entails a pronounced pH buffering effect during equilibration in this carbonate dominated chemical system. This is supported by the overall high pH values (8.1 to 8.8; Table 3) measured in the modern waters at Erzberg. The efficient dissolution of the carbonate host rocks by sulphuric acid, as well as the related outgassing of CO₂ (Eqs 3 and 4) and concomitant precipitation of aragonite-calcite in open fractures (Eq. 5 below), will lead to relatively high (buffered) pH values. Silicate weathering (hydrolysis of silicates) could also play a (minor) role with regard to some pH buffering capacity at lower pH conditions. Variable K (up to 10 mg l⁻¹) and Al concentrations (up to 63 µg l⁻¹; Table 3) might be indicative of this chemical process. Some of the widespread accessory silicate minerals detected in the carbonate host rocks (Table S1) showed a partially altered (corroded) appearance under the microscope. The process of calcium carbonate vein mineralization in fractures can be described by the overall reaction:



Importantly, pronounced CO₂ outgassing from the evolving aqueous solutions in the course of sulphuric acid based dissolution, oxidative weathering of iron carbonate and CaCO₃ precipitation in fractures (Eqs 2 to 5) can explain the prominently high δ¹³C values (up to +7‰ VPDB; Fig. 5) found in erzbergite, i.e. stable C isotopic compositions significantly increased compared to their carbonate source rocks. The occurrence of kinetic enrichment in DIC during preferred degassing of isotopically light ¹²C¹⁶O₂ (Michaelis *et al.*, 1985; Mickler *et al.*, 2006; Scholz *et al.*, 2009) is supported by the high δ¹³C_{DIC} values (2.4 to 3.8‰ VPDB; Table 3) analyzed in modern Erzberg waters. Moreover, an enhanced potential regarding CO₂ outgassing is clearly

suggested by the high log_PCO₂ of -3.2 to -2.3 of the aqueous solution and high CaCO₃ supersaturation (SI_{Arag} 0.7 to 1.3; SI_{Cc} 0.8 to 1.4) calculated from the modern hydrochemistry (Table 3). Degassing, stable isotopic enrichment and concomitant calcium carbonate precipitation could be further influenced by turbulent flow regimes (vadose waters) or evaporation effects (also increasing δ¹⁸O of waters and precipitates) mostly in fractures and water flows near the surface (*cf.* Koltai *et al.*, 2017).

Local differences in hydrochemistry and erzbergite formation

Hydrochemical relationships

The hydrochemical composition of modern water collected at Erzberg (Table 3) revealed distinct spatial differences and can be grouped into southern, central and northern sections of the open pit mine (Fig. 1). The vast majority of the erzbergite encountered on-site originates from the southern part of the mountain range (Fig. 1). The spatial differentiation is manifested in various relations of hydrochemical parameters measured (plots shown in Figs S2 and 6). Different hydrochemical groups are reflected in the distinct water types, i.e. dominantly Mg-HCO₃ (south), Mg-Ca-HCO₃-SO₄ (central) and Mg-Ca-HCO₃ (north). The sampling site Oberegger-South (sample WEB4; Table 3) yielded more intermediate compositions. Obviously, the waters sampled reflect different genetic characteristics and stages of hydrochemical evolution, and consequently different potentials for local vein (CaCO₃) formation.

Waters from the southern Erzberg section mostly yielded lower EC values and Ca concentrations at higher pH than elsewhere, probably resulting from more pronounced CaCO₃ precipitation (Fig. 6A and B). In contrast, the modern waters from the central section have significantly higher EC and Ca contents (up to 107 mg l⁻¹) at lower pH due to higher ion (carbonate and sulphate) contents in solution there (Table 3; Fig. 6). The validity of this principal hydrochemical connection is supported by lower CO₂ partial pressures (log_PCO₂ around -3 atm; Fig. S2A) in aqueous solutions of the southern section compared to significantly higher P_{CO2} around -2.5 calculated for the more central section. In spite of the overall high CO₂ outgassing potential of these waters, the southern samples depict more pronounced degassing and CO₂ partial pressures closer to atmospheric

values ($\log P_{\text{CO}_2}$ around -3.4 atm), while the central samples still hold a higher degassing and CaCO_3 precipitation potential. Increased southern CO_2 degassing can also be inferred from the more positive $\delta^{13}\text{C}_{\text{DIC}}$ compositions analyzed (Table 3). This interpretation is also supported by a distinct positive correlation of the Ca versus P_{CO_2} values (Fig. S2A); Ca concentrations are decreased (carbonate precipitation progressed) at reduced (degassed) CO_2 contents and vice versa. A more advanced hydrochemical evolution with respect to carbonate precipitation in the southern Erzberg section is also in line with lower aragonite and calcite supersaturation calculated for these waters (Table 3). The observations further correspond well to prominently reduced Sr and Ba concentrations measured in waters of the southern section (Table 3). These elements are known to be incorporated in the course of predominant precipitation of aragonite, and prior aragonite precipitation (Dietzel *et al.*, 2004; Jones, 2017).

Incongruent host rock dissolution and Mg/Ca evolution

Magnesium hydrochemical contents are conspicuously high in the southern and central sections (*ca* 100 to 155 mg l^{-1} ; Table 3) and a plot of the molar Mg/Ca versus Ca

concentrations displays two principal groups of carbonate host rock dissolution versus successive carbonate precipitation (Fig. 6C). In the first group (central and north, also sample WEB4), the molar Mg/Ca ratios (2 to 3) are significantly enriched but relatively constant, suggesting a major influence of a Mg-rich carbonate source, i.e. ankerite (often >10 wt% MgO), dolomite or Mg-limestone dissolution. The second group (dominantly south) is characterized by strongly decreased Ca contents at strongly increased molar Mg/Ca ratios (up to 26; Fig. 6C). This can be interpreted as successive relative enrichment of Mg versus Ca in aqueous solution depending on prior calcium carbonate precipitation (decreasing dissolved Ca and carbonate alkalinity along the flow path). The prevailing mineralization of aragonite (repelling Mg from the crystal lattice) will lead to increased Mg/Ca ratios and is thus another important indicator of a more advanced hydrochemical evolution in the southern Erzberg section than elsewhere. Constant Mg/Ca molar ratios of waters from the central and northern area were coupled to constant molar Mg versus HCO_3^- ratios of around 0.5 there (0.3 to 0.6; north lowest; Fig. S2B). This clearly suggests a near constant stoichiometry with balanced carbonate dissolution and precipitation

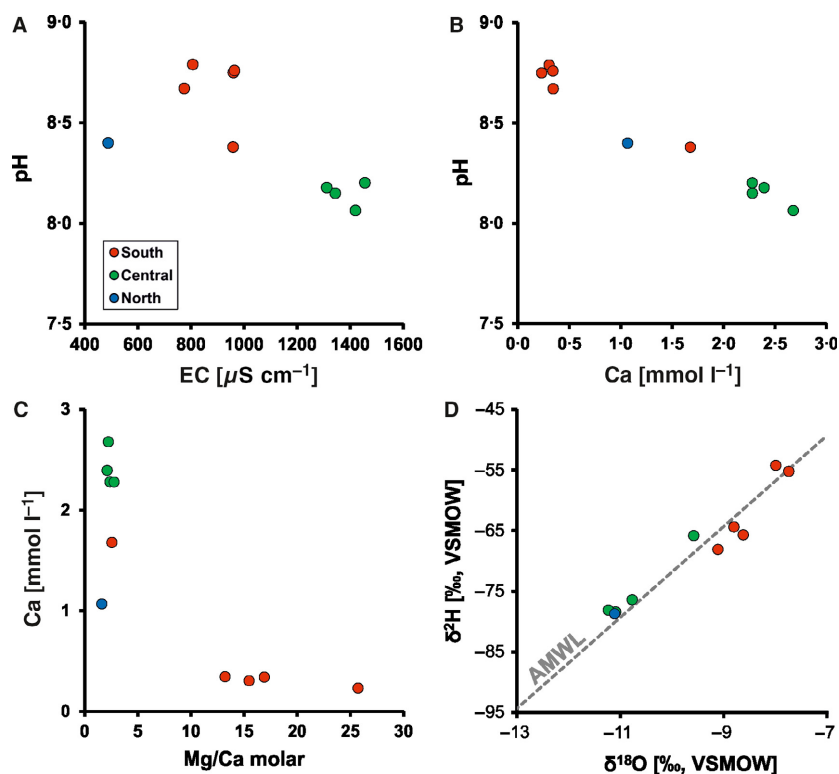
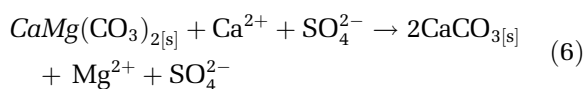


Fig. 6. Hydrochemical relationships of modern waters from Erzberg displaying spatial differences between southern, central and northern sampling sites (data points of different colours). (A) Electric conductivity versus pH. (B) Ca concentration versus pH. (C) Molar Mg/Ca ratio versus molar Ca concentration. (D) $\delta^{18}\text{O}$ versus $\delta^2\text{H}$ compared to the Austrian Meteoric Water Line ($\delta^2\text{H} = 7.5 \cdot \delta^{18}\text{O} + 3.2$).

involving a major magnesium carbonate source. A common hydrochemical mechanism in carbonate aquifers consists of the incongruent dissolution (de-dolomitization) of Mg-rich host rocks; for example, the dissolution of ankerite or dolomite and the concomitant precipitation of calcite or aragonite (Hanshaw & Back, 1979; Mittermayr *et al.*, 2017). This is essentially based on the different solubilities and kinetic mineralization potential of these minerals, i.e. the slow dissolution of dolomite or ankerite and concomitant supersaturation and kinetically-favoured precipitation of CaCO_3 (dominantly aragonite at Erzberg) following the overall exchange reaction:



Incongruent Mg-bearing carbonate dissolution followed by aragonite precipitation yields the potential for a pronounced increase of Mg/Ca in the aqueous solution. At Erzberg, the excessive Ca needed for the promotion of the incongruent dissolution reaction primarily originates from the occurrence of sulphide oxidation entailing efficient sulphuric acid production and carbonate dissolution (and increased sulphate contents). In principle, additional Ca could also result from the dissolution of Ca-sulphates (gypsum or anhydrite; Hanshaw & Back, 1979).

Meteoric water infiltration

Spatial characteristics evolving from the particular water infiltration area, flow routes, seasonal and spatial mixing, as well as interaction and residence time in the aquifer can also be inferred from the water stable H and O isotopic compositions (Fig. 6D). The broad range of $\delta^2\text{H}$ (-78.7 to -54.3‰ VSMOW) and $\delta^{18}\text{O}$ (-11.2 to -7.7‰ VSMOW; Table 3) measured in the Erzberg waters allows differentiation of the meteoric waters between the southern, central and northern section. All of the waters clearly indicate a meteoric origin based on their H versus O isotopic distribution close to the Austrian Meteoric Water Line (AMWL in Fig. 6D; Hager & Foelsche, 2015). The consistently higher $\delta^2\text{H}$ and $\delta^{18}\text{O}$ values of the southern waters could result from an infiltration area of lower altitude or from a higher proportion of warm season rainfall in contrast to cold season rain or snow (melt). A potential seasonal influence is supported by the pronounced seasonal amplitude of

ca 10‰ in $\delta^{18}\text{O}$ of regional meteoric precipitation (data from nearby meteorological station Wildalpen; Umweltbundesamt, 2017). Another feature of the southern waters is their overall lower deuterium excess (Table 3), reflecting a slightly enriched O isotope signature relative to the AMWL (Fig. 6D). Central and northern waters showed typically lower $\delta^2\text{H}$ and $\delta^{18}\text{O}$ values (Fig. 6D) probably indicative of a higher elevation of the principal meteoric water infiltration area. Alternatively, these waters could involve a higher proportion of cold season rain or infiltrated snowmelt (in line with a higher infiltration area). The waters further yielded an overall higher deuterium excess compared to the southern section (Table 3). In general, however, the average deuterium excess value (3.5) is very similar to the value reported for the AMWL (3.2; Hager & Foelsche, 2015). The northern water seems genetically related (diluted) to the central waters. Water residence times in the dominantly fissured aquifer are considered to be short (months to a few years), although not investigated in detail. Importantly, the finding of sulphide oxidation and sulphuric acid evolution supports an efficient mechanism of host rock dissolution explaining the overall high solute contents of the Erzberg waters without the necessity for extensive residence times. In essence, the modern hydrochemistry at Erzberg is still favourable for ongoing erzbergite formation irrespective of the anthropogenically disturbed water flow regimes from the mining activities.

Aragonite–calcite and lamination

CaCO₃ polymorphism

The polymorphism of its calcium carbonate minerals (aragonite and calcite) constitutes a characteristic feature of erzbergite. The layered (laminated or banded) precipitates are dominated by aragonite, which is mainly attributable to the prominently elevated Mg/Ca ratio in the erzbergite precipitating solutions. Magnesium is well-known to promote aragonite instead of calcite nucleation and crystal growth in comparable low (ambient) temperature natural or laboratory experimental settings (Riechelmann *et al.*, 2014; Rossi & Lozano, 2016; Purgstaller *et al.*, 2017). Modern waters at Erzberg yielded high Mg concentrations with up to 153 mg l⁻¹ measurable depending on the particular hydrogeochemical evolution path. Molar Mg/Ca ratios of 2 : 1 up to 26 : 1 in the modern waters are high and more

enriched in the southern Erzberg section, where most of the erzbergite samples were found. Based on different studies considering aragonite versus calcite precipitation, molar Mg/Ca ratios exceeding between 1 and 3 (Frisia *et al.*, 2002; Dietzel *et al.*, 2004; Rossi & Lozano, 2016; Spötl *et al.*, 2016; Jones, 2017) were reported as thresholds for aragonite superseding calcite formation at normal ambient surface temperature. The occurrence of Mg-calcite in the aragonite-dominated erzbergite precipitates constrained by EPMA–WDX mapping and spot analyses (Fig. 4), as well as XRD peak positions reinforces the view that high but variable Mg concentrations affected the precipitating CaCO₃ polymorph. Elevated Mg in the fracture water is closely related to the occurrence of particular carbonate host rocks such as ankerite, Mg-rich limestone or (Fe-) dolomite at Erzberg. The fact that prior aragonite or calcite precipitation increased the aqueous Mg/Ca ratios is also supported by the consistently high erzbergite $\delta^{13}\text{C}$ values (preferential outgassing of isotopically light $^{12}\text{CO}_2$ and enrichment of $\delta^{13}\text{C}_{\text{DIC}}$; Bajo *et al.*, 2017). Prior aragonite precipitation would further explain the lower Sr and Ba concentrations in waters of the southern Erzberg section (Table 3), i.e. these minor elements are readily incorporated into aragonite compared to the small Mg²⁺ cation (Böttcher & Dietzel, 2010). Similarly, (prior) aragonite precipitation would also diminish the overall uranium concentration in aqueous solution based on the respective fractionation behaviour (Wassenburg *et al.*, 2016) and might be the explanation for low to very low U contents measured in some erzbergite samples (Table 1). Most of these hydrogeochemical mechanisms proposed are known to depend on water infiltration, flow routes and discharge, such that aqueous Mg/Ca increases related to prior CaCO₃ precipitation are typically favoured during overall dry environmental/aquifer conditions (Huang & Fairchild, 2001; Riechelmann *et al.*, 2014; Bajo *et al.*, 2017). The low discharge of modern water encountered in fractures at Erzberg supports this conclusion. Elevated dissolved sulphate contents (up to 226 mg l⁻¹) could also contribute to dominant aragonite over calcite nucleation, i.e. sulphate has been discussed as an inhibitor of calcite precipitation (Busenberg & Plummer, 1985; Rodriguez-Navarro & Benning, 2013).

Other factors arguing for aragonite precipitation comprise the prominently high CaCO₃ saturation states calculated from the waters monitored, i.e. saturation indices of up to 1.3 (mean = 0.9) for aragonite reflecting a

pronounced fluid–solid interaction and hydrochemical evolution. These saturation states are even higher compared with other studies in which low temperature aragonite formation was observed (Riechelmann *et al.*, 2014; Spötl *et al.*, 2016). A general definition of a critical CaCO₃ saturation state promoting aragonite, however, seems difficult to ascertain (Rossi & Lozano, 2016). Depending on the prevailing CO₂ partial pressures (solution versus atmosphere) pronounced CO₂ degassing was reported to potentially trigger aragonite nucleation irrespective of the particular Mg/Ca ratios (Jones, 2017). Considering the limited vadose water flow observed in fractures and on surfaces, evaporation could also have an effect on the potential for aragonite nucleation (Frisia *et al.*, 2002; Koltai *et al.*, 2017). Regarding evaporation effects, it should be considered that the original aqueous solutions and accompanying (humid) atmosphere from which erzbergite was precipitated were more or less distant from the current (mining) surface and its direct influences. Further, based on O and clumped isotope analyses, erzbergite was precipitated from meteoric waters at low temperatures (Table 2) clearly negating a dominant temperature trigger or even erzbergite formation from thermal waters or hypogenic sources. Organic macromolecules or microbial activity could also have contributed to preferential aragonite nucleation (Niedermayr *et al.*, 2013; Jones, 2017). Regarding a significant active or passive influence of biological processes on CaCO₃ crystallization (for example, comparable to travertine; Jones, 2017), this study found no petrographic evidence in the vast proportion of the erzbergite veins. In two samples, scarce indications of some microbial (biofilm) presence exists (Fig. S1I and J).

Lamination and zonation

Most erzbergite samples investigated show some kind of layering manifested as (sub) millimetre-scale lamination patterns or as centimetre-scale banding patterns (zonation; Fig. 2). Laminated samples are characterized by the recurrent deposition of Fe-rich (goethite) brownish stained particle layers (for example, samples EB1, EB3 and parts of EB6; Figs 2 and 3). Samples of persistently homogeneous zonation are characterized by either a constant mineralogy consisting of snow white to slightly brownish stained aragonite (for example, sample EB7; Fig. 2F to H) or by extensive diagenetic alteration resulting in a different macroscopic colouring and more compact

fabric (for example, beige and dense calcitic replacement of EB22; Fig. 2E). The prominent narrow lamination is an original growth feature. The occurrence of original (Mg-) calcite is of minor relevance, i.e. extended environmental conditions of calcite precipitation are obviously restricted (inhibited) at Erzberg. Most Mg-calcite layers detected were associated with stained particle layers (Figs 3 and 4).

Regarding the origin of the lamination and zonation, a regular annual (seasonal) control proposed in earlier studies discussing erzbergite formation (Hatle, 1892; Angel, 1939) seems unlikely for the investigated samples. Mineralogical and petrographic observations in this study, in combination with radiometric U-Th dating, suggest an overall irregular nature and recurrence intervals of the typical layering in erzbergite. This is the case for aragonite versus calcite, as well as for the intercalated stained (Fe-rich) particle layers. The latter, however, show high-frequency recurrence intervals in a few of the samples investigated (for example, sample EB3; Figs 3G, 3H and 4), i.e. these detrital particle layers might reflect some seasonal rhythm (for example snowmelt). Considering their aragonite–calcite relation and detrital particle input, the erzbergite deposits are significantly different from other aragonite–calcite precipitates recently reported from non-karstic fractures in the Alps (Koltai *et al.*, 2017). The irregular layering of the erzbergite fracture fillings primarily reflects the prevailing environmental and hydrochemical conditions on different timescales (seasons to millennia). Sample EB2, for example, comprises two major and chronologically clearly separated growth intervals showing distinct bidirectional growth towards complete fracture filling, i.e. also expressed in the petrographic zonation (Fig. 7). The lamination (shorter-term) and banding (longer-term) are probably also spatially (locally) different, i.e. between different fractures or along extensive fractures. In principle, the relevant hydrochemical and mineral deposition mechanisms strongly rely on the availability and amount of water in the fractures at Erzberg. Consequently, the lamination from stained detrital particle layers could be an expression of increased host rock weathering and mobilization in the course of increased aquifer recharge and discharge (wet intervals or flushing events; for example, snowmelt, heavy rain periods or cycles of wetter climate). Based on the comparison of multiple successive U-Th data and the corresponding petrography (for example, sample EB2;

Fig. 7), the erzbergite growth dynamics revealed no evidence of partially condensed (restricted) CaCO₃ precipitation favouring a narrow and visually enhanced (stained) layering (e.g. Boch & Spötl, 2011). The restricted occurrence of original (Mg-) calcite laminae could be related to transient wetter conditions reducing the effects of prior CaCO₃ precipitation and CO₂ outgassing. Considering the intervals (bands) of homogeneous mineralogy (mostly aragonite), this clearly suggests a prevailing ('normal') mode of erzbergite precipitation, i.e. environmental conditions preferring aragonite over calcite. This dominance, however, does not exclude the occurrence of significant variations in temperature, isotopic and trace elemental compositions. The common replacement of aragonite with calcite probably results from dissolution of aragonite and re-precipitation of low-Mg calcite. The necessary presence of water could be provided by remnant parent fluid inclusions in pore spaces (Figs S1A and 3A) or via the later percolation of fracture water into microscopic pores and cracks (for example, sample EB1, Fig. S1H).

Temperatures of aragonite formation

The clumped isotope measurements of selected aragonite subsamples yielded cool formation temperatures of <10°C (± 2 to 8°C; Table 2). These values are even lower than the water temperatures measured in the modern fracture and surface waters during the warm season (Table 3). Indeed, the erzbergite precipitates represent a rare case of geologically young aragonite precipitation at low to near-freezing temperature conditions (Rossi & Lozano, 2016; Spötl *et al.*, 2016). Aragonite precipitation from aqueous solutions of meteoric origin is supported by the O isotopic composition of all erzbergite samples (Table S3; Fig. 5), as well as by the stable H and O isotopic composition of the modern waters (Table 3; Fig. 6D). In particular, the cool (water) temperatures most likely reflect the cool Alpine setting at Erzberg and the high elevation of the meteoric water infiltration area (*ca* 1500 m a.s.l. or even higher in the adjacent areas; see Fig. 1). Mean annual air temperatures reported from the Wildalpen meteorological station near Erzberg (610 m a.s.l.) are *ca* 6°C (monthly data from 1984 to 1997; Umweltbundesamt, 2017). Based on the established altitude gradient of *ca* $-0.5^{\circ}\text{C}/100\text{ m}$ this can be roughly translated into a mean annual air temperature of *ca* 2°C at the top of Erzberg (1532 m originally; 1466 m today). Next to the

altitude, the prevailing overall climate conditions during erzbergite precipitation might exert a major influence. Similarly, the pronounced seasonality and seasonal weighting of water infiltration are also highly relevant. At Wildalpen, the annual average of meteoric precipitation amounts to *ca* 1500 mm (monthly data from 1972 to 2002; Umweltbundesamt, 2017) in which the variability of convective rainfall during summer (thunderstorms), and advective precipitation (Atlantic versus Mediterranean) and the magnitude of snowmelt after winter might be determining with regard to aquifer recharge.

Additional environmental information on the past aqueous solution source and composition can be derived from the clumped isotope measurements, i.e. the palaeofluid $\delta^{18}\text{O}$ can be calculated from the carbonate formation temperature and simultaneously measured aragonite O isotopic composition assuming equilibrium fractionation (Eiler, 2007; Kluge *et al.*, 2015). Based on

the clumped isotope analyses (Table 2) and available aragonite versus aqueous solution fractionation factors (Zhou & Zheng, 2003; Kim *et al.*, 2007) fluid $\delta^{18}\text{O}$ values ranging from -10.7 to -7.5‰ VSMOW (Zhou & Zheng, 2003) or -11.8 to -8.7‰ VSMOW (Kim *et al.*, 2007) can be inferred. Thus, the clumped isotope derived fluid $\delta^{18}\text{O}$ values show an approximated overall range of -12 to -7‰ VSMOW depending on the erzbergite sample and fractionation factor used. Modern water from Erzberg sampled during the warm season (spring/summer) revealed average $\delta^{18}\text{O}$ values of -9.6‰ VSMOW (Table 3) in which the southern Erzberg section waters showed higher values (-9.1 to -7.7‰) relative to the central section (-11.2 to -9.6‰ ; Table 3). Consequently, the isotope analyses of modern water from both sections revealed a similar range in comparison with the clumped isotope based erzbergite precipitating fluid $\delta^{18}\text{O}$. Monthly water isotope data (H and O) of regional meteoric precipitation

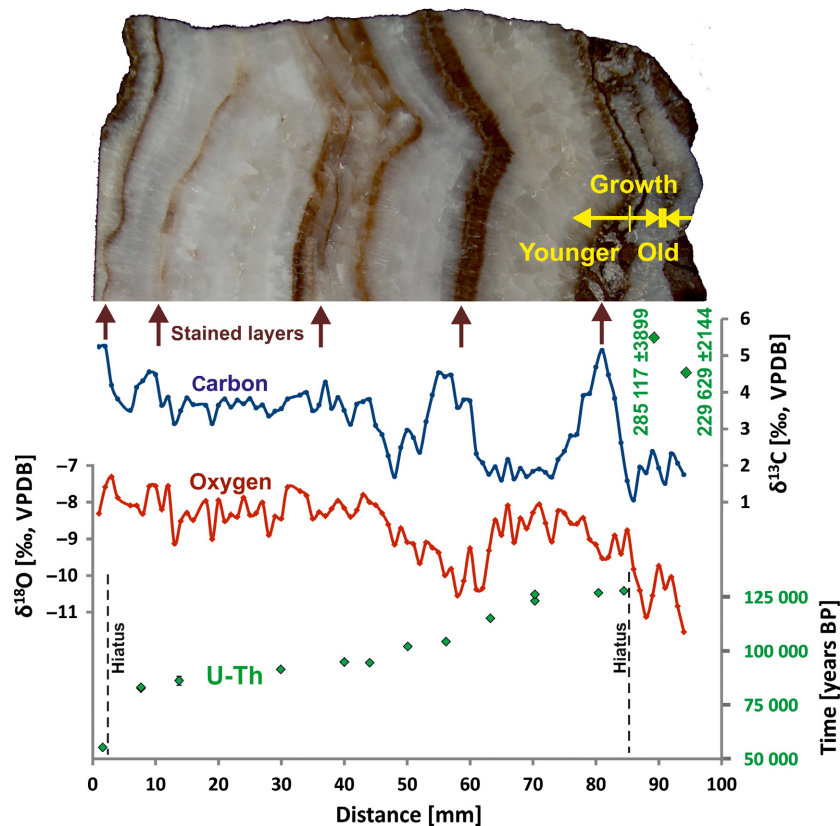


Fig. 7. Stable C and O isotope transects of sample EB2 plotted against the petrography and radiometric U-Th age data (green rhombs; 2σ age uncertainties mostly smaller than symbols). An older interval (between *ca* 285 kyr and 230 kyr BP) of bidirectional growth can be distinguished from a younger depositional interval (*ca* 128 to 55 kyr BP) of unidirectional erzbergite precipitation (yellow arrows). Two major growth interruptions (hiatus – dashed lines) demarcate a dominant sample section of overall rather constant growth. Several prominent brownish stained layers show some spatiotemporal correspondence to high $\delta^{13}\text{C}$ values (brown arrows).

(Wildalpen meteorological station; Umweltbundesamt, 2017) including data from the Austrian Network of Isotopes in Precipitation (ANIP; Hager & Foelsche, 2015) report mean annual $\delta^{18}\text{O}$ values of -11.4‰ (VSMOW), warm season compositions of *ca* -9.0‰ and cold season averages of *ca* -13.6‰ for the time interval from 1976 to 2015. Taking a $\delta^{18}\text{O}$ versus altitude gradient of $-0.19\text{‰}/100\text{ m}$ (Hager & Foelsche, 2015) and a Wildalpen versus Erzberg altitude difference of *ca* 900 m into account, the mean annual $\delta^{18}\text{O}$ of meteoric precipitation at the top of Erzberg can be approximated to -13.1‰ (VSMOW). Accordingly, the warm season values are translated to -10.7‰ and the corresponding cold season values calculated average -15.3‰ . Thus, the erzbergite fluid $\delta^{18}\text{O}$ values inferred from the clumped isotope analyses (*ca* -12 to -7‰) show a rather similar O isotopic composition range relative to today's warm climate conditions. Especially, the inferred (parental fluid) values are either close to the modern annual average or tend towards the warm season meteoric precipitation compositions, i.e. lower values approximate today's annual average and higher values reflect warm season infiltration and/or local evaporation. In essence, the aragonite formation temperatures and corresponding aqueous solution $\delta^{18}\text{O}$ values strongly suggest preferred erzbergite formation during comparatively warm (and wet) local climate and/or seasonal conditions at this generally cool (high altitude) Alpine setting. During overall cool (and dry) climate and/or seasonal conditions erzbergite formation and water availability were probably strongly restricted by temperatures falling below freezing. The latter implications are further supported by a comparison with radiometric U-Th age determinations (Fig. 8). Subsample EB1-CI1 ($4 \pm 3^\circ\text{C}$; Table 2) precipitated between $102.3 \pm 0.6\text{ kyr}$ (average of two U-Th ages) and $97.3 \pm 0.6\text{ kyr BP}$ (Table 1) while subsample EB1-CI2 ($2 \pm 8^\circ\text{C}$) is slightly younger than a nearby U-Th sample of $77.3 \pm 1.6\text{ kyr BP}$ in age (Table 1). Thus, the two EB1 samples represent aragonite formation during MIS 5.3 and MIS 5.1, respectively (Fig. 8), i.e. relatively warm and wet climate intervals (interstadials) during the (early) Last Glacial period. Likewise, clumped isotope sample EB6-CI1 ($3 \pm 5^\circ\text{C}$; Table 2) was extracted near (slightly younger) a U-Th age constraint of $14.7 \pm 0.3\text{ kyr BP}$ (Table 1) and formed around the start of the Late Glacial Bölling/Alleröd warm period (B/A; e.g. Björck *et al.*, 1998; Fig. 8). This is also the case for sample EB12-CI1 ($8 \pm 2^\circ\text{C}$); the subsample itself was

U-Th dated representing aragonite precipitation in the early phase of the B/A warm period ($14.17 \pm 0.19\text{ kyr BP}$). Another subsample from EB12 (EB12-CI2, $9 \pm 4^\circ\text{C}$) was directly dated to $4.99 \pm 0.24\text{ kyr BP}$ (Table 1), i.e. the relatively warm and wet mid-Holocene climate interval (Fig. 8). Sample EB7-CI1 ($3 \pm 7^\circ\text{C}$) also supports aragonite deposition during the relatively warm/wet early to mid-Holocene (between $10.41 \pm 0.17\text{ kyr}$ and $3.27 \pm 0.07\text{ kyr BP}$; Table 1). Similarly, sample EB21-CI1 ($5 \pm 4^\circ\text{C}$; Table 2) formed during the early Holocene (directly dated; $9.48 \pm 0.09\text{ kyr BP}$).

Fracture formation and palaeoenvironmental archive

Implications on open fractures

Based on the processes and erzbergite growth dynamics presented, further environmental implications can be drawn. Obviously, the opening of fractures as a result of tectonic or gravitational mass movements is a prerequisite for the deposition of aragonite–calcite fillings, i.e. providing (vadose) water flow routes in the fissured aquifer. The open fractures of variable width and length imply fresh chemical reaction surfaces of the host rock carbonates and its sulphide accessories. This promotes sulphide oxidation, carbonate dissolution, mobilization and finally precipitation, i.e. the hydrochemical mechanism of erzbergite formation and the associated closing ('healing') of the fractures is initiated more or less immediately. The latter mainly depends on the availability and percolation of meteoric water (for example, warm and wet conditions). A major relevance of open fractures in the course of deep-seated gravitational slope deformations or brittle fault zones with regard to fluid–solid interaction was also mentioned in other studies from the Alpine realm (Strauhal *et al.*, 2016; Koltai *et al.*, 2017). Numerous and precise radiometric U-Th measurements yielded young ages for the fracture fillings, i.e. late Pleistocene, and all of the samples collected *in situ* are younger than the Last Glacial Maximum (*ca* $<20\text{ kyr BP}$; Table 1; Fig. 8). The young ages of erzbergite further argue for the reliability of the U-Th data with respect to chemical alteration effects during eventual diagenetic replacement of aragonite, i.e. preferential loss of U would result in systematic age offsets towards older ages (Ortega *et al.*, 2005; Lachniet *et al.*, 2012). The carbonate precipitates therefore strongly support geologically young and mostly short time intervals of complete infilling. In this

study, it is also considered unlikely that the fractures themselves are much older, i.e. they have not rested open over extended time intervals with closure much later. In light of these structural versus hydrogeochemical relationships, the radiometric age determination of aragonite–calcite veins thus holds future potential for spatiotemporal investigation of fracture development at Erzberg, for example, gravitational versus (neo)tectonic causes.

Palaeoclimate reconstruction

This study's geochemical investigation of erzbergite suggests an interesting potential for palaeoenvironmental reconstructions. Various petrographic, elemental and isotopic parameters (environmental proxies) archived in these chemical sediments strongly depend on the prevailing environmental conditions in a climate-sensitive Alpine setting. Importantly, the specific climate

information can be assessed in a reliable time-frame based on precise U–Th radiometric dating (absolute timing and rates of change) and the latter clearly revealed that aragonite–calcite precipitation in the fractures is tied to favourable (warm and wet) environmental and hydrochemical conditions (Fig. 8). The clumped isotopic composition of erzbergite carbonate has been shown to represent a promising tool for studying regional temperature changes of the past. Valuable information on the prevailing palaeotemperatures is further archived in the distinct O isotope variability of erzbergite samples from different time/climate intervals (Figs 5 and 7). An intimate connection of air temperature and $\delta^{18}\text{O}$ of meteoric precipitation is well-established in the Austrian Alps (Hager & Foelsche, 2015). The O isotopes in the CaCO_3 precipitates are further influenced by seasonally weighted contributions of warm versus cold season water infiltration. Also, the

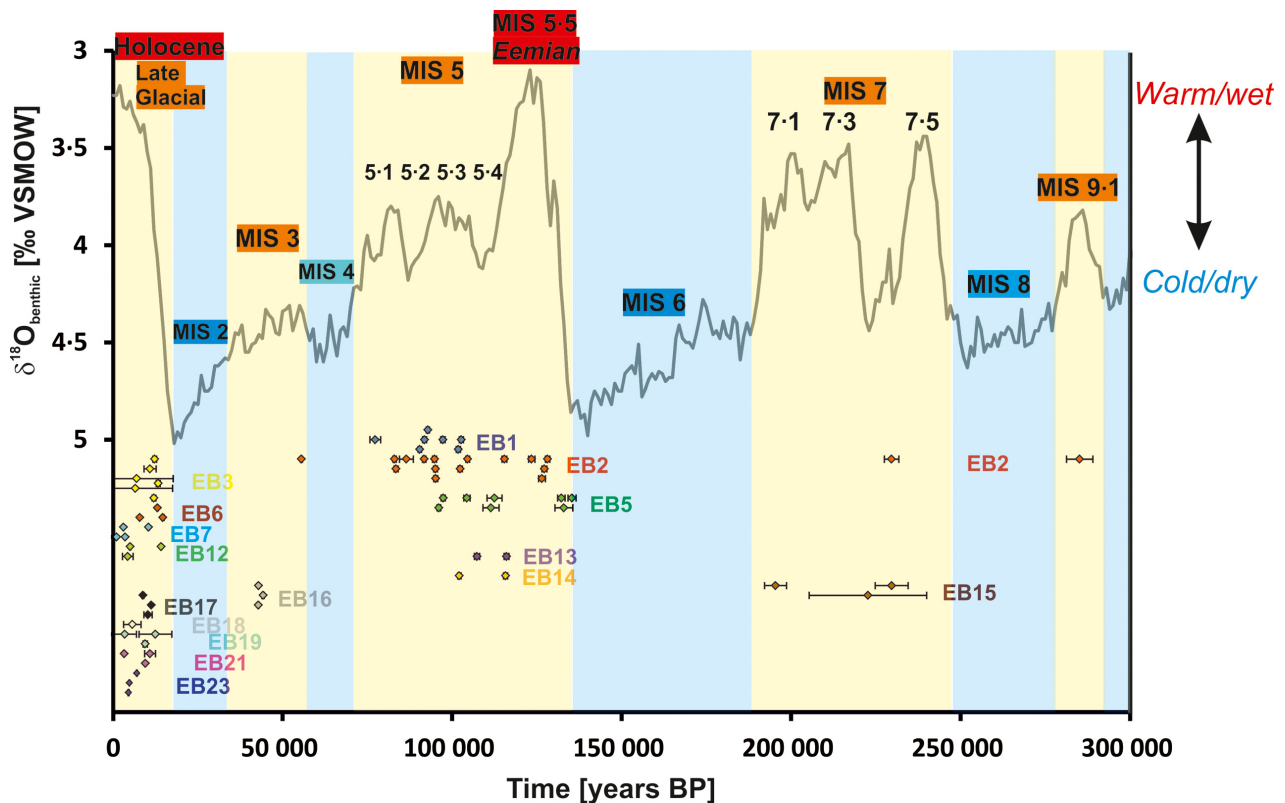


Fig. 8. Uranium–thorium based ages of different erzbergite (samples EB1 to EB23) carbonate precipitates in fractures (rhombs with 2σ age uncertainties) plotted against the marine (benthic) stable O isotopic evolution of the last 300 kyr BP (grey curve; after Lisiecki & Raymo, 2005). Erzbergite formation is clearly favoured during overall relatively warm and wet climate intervals (water availability; yellow areas highlighting times dominated by interglacials and intermittent interstadials), for example, Marine Isotope Stages (MIS) 9-1, 7, 5-5 (Eemian), 5, 3, the Late Glacial transition and the Holocene up to modern times (red and orange labels). In contrast, none of the U–Th data points plot within the overall relatively cool and dry climate intervals (major cold glacials and cool stadials; bluish areas and MIS labels), for example, MIS 8, 6, 4 and 2 (Last Glacial Maximum).

extent and timing of snowfall and subsequent snowmelt or the variable advection of moist air masses (Atlantic versus Mediterranean) are probably of high relevance. Additional palaeofluid composition and related palaeoclimate information could be archived in the form of fluid inclusions trapped in (parts of) the erzbergite carbonate (Demény & Siklósy, 2008; Dublyansky & Spötl, 2009). Increasing carbonate $\delta^{13}\text{C}$ values are influenced by enhanced prior CaCO_3 precipitation or could also result from CO_2 production and partial degassing in the course of siderite corrosion and sulphuric acid dissolution of ankerite, dolomite or calcite (Eqs 2 to 4). These hydrogeochemical processes could be enhanced during overall drier environmental and aquifer conditions (reduced flow and increased residence times) and further determine some of the minor and trace elements (Mg, Sr, Ba and U), i.e. another proxy of meteoric palaeoprecipitation (*cf.* Wassenburg *et al.*, 2016). Regarding potential palaeoclimate information from the erzbergite mineralogical composition and lamination, the stained Fe-rich particle accumulations probably represent increased mobilization during wet episodes, for example seasonal or multi-annual flushing events supported by the detrital nature of the stained layers. Thus, they could be the expression of increased seasonality and overall more extreme conditions (alternating wet versus dry aquifer conditions).

CONCLUSIONS

This study is focused on a detailed geochemical and petrographic characterization of erzbergite precipitates complemented by modern aqueous solution analyses at Erzberg, and is aimed at a better process understanding of carbonate growth dynamics and environmental dependencies (Fig. 9). Major results and implications include:

1 Formation mechanisms – Cool meteoric water infiltration and accessory sulphide oxidation constitute the principal hydrochemical reaction mechanism of efficient (Ca, Mg and Fe) carbonate host rock dissolution, mobilization and subsequent aragonite–calcite precipitation in vertical fractures. This is constrained by persistently high $\delta^{13}\text{C}$ values of the erzbergite and dissolved inorganic carbon, as well as high sulphate concentrations and indicative sulphur stable isotopic compositions of modern waters. The first clumped isotope measurements

conducted at Erzberg yielded cool formation (water) temperatures of <10 (± 5) $^\circ\text{C}$ for the erzbergite (aragonite) precipitates in fractures. This rare case of aragonite precipitation at low to near-freezing temperature conditions primarily reflects the cool Alpine setting and high altitude of the meteoric water infiltration area, together with the overall prevailing climate conditions during erzbergite precipitation. Parental fluid $\delta^{18}\text{O}$ compositions inferred from the clumped isotope aragonite $\delta^{18}\text{O}$ data and temperature constraints revealed rather similar O isotopic compositions of the palaeowaters relative to today. Erzbergite formation is promoted during generally warm (and wet) climate and/or seasonal environmental conditions at Erzberg and restricted by recurrent freezing conditions in this overall cool setting.

2 Age of erzbergite – Multiple radiometric ^{238}U – ^{234}U – ^{230}Th dating resulted in young ages of the fracture veins dated so far, i.e. 285.1 ± 3.9 to 1.03 ± 0.04 kyr BP. All of the samples collected on-site are younger than the Last Glacial Maximum. Typical relative age uncertainties (2σ) amount to 0.5 to 1.0% (absolute errors of \pm few hundreds of years). Average erzbergite growth rates are on the order of a few tens of micrometres per year corresponding well to the cool (higher altitude) Alpine setting.

3 Polymorphism – Erzbergite veins are clearly dominated by aragonite relative to original as well as diagenetic (Mg) calcite, i.e. hydrochemical conditions favouring aragonite instead of calcite precipitation represent the prevailing ('normal') mode of erzbergite formation. The CaCO_3 polymorphism is mainly controlled by the high Mg/Ca ratios of the erzbergite depositing solutions (inhibiting calcite nucleation), intense fluid–solid interaction (high total dissolved solid and SI values) involving Mg-rich host rocks and a hydrochemical evolution involving prior CaCO_3 precipitation in the fissured aquifer.

4 Layering – The lamination (millimetre-scale) and zonation (centimetre-scale) patterns characteristic of erzbergite precipitates are primarily the result of a variable mineralogy. The lamination is an original depositional feature mainly associated with stained (Fe-rich) detrital particle layers. The broader zonation (banding) reflects a constant mineralogy in most cases. In some cases, it results from partial diagenetic replacement of aragonite towards calcite having a different colouring and fabric. Petrographic observations in combination with radiometric U–Th dating

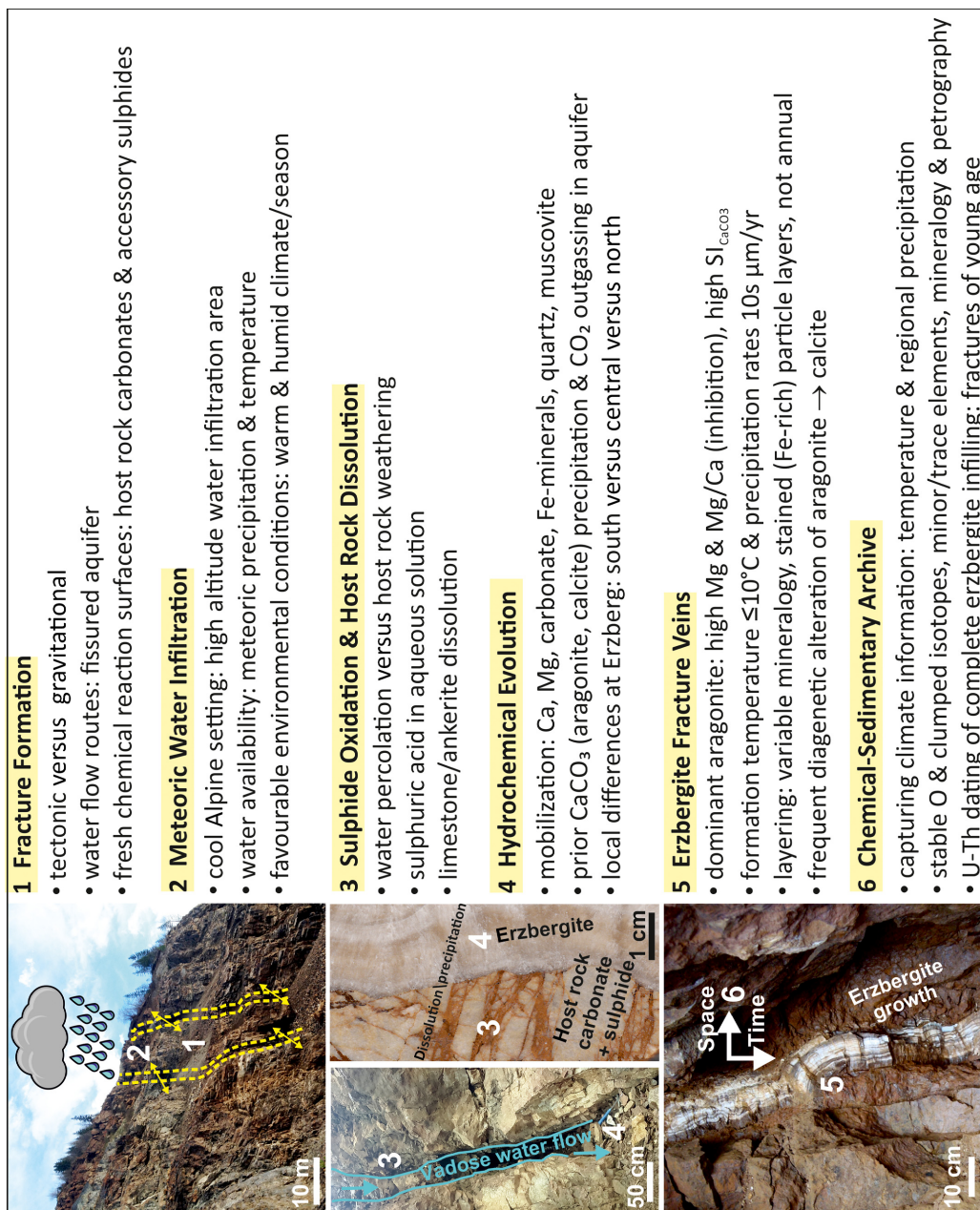


Fig. 9. Conceptual and stepwise (1 to 6) compilation of erzbergite carbonate precipitation in vertical fractures at Erzberg. Large-scale and small-scale physicochemical processes are closely related, and the precipitates capture variable environmental conditions in their chemical and petrographic composition.

suggest an overall irregular nature and recurrence intervals of the layering. Few samples show intervals of regular (seasonal) lamination.

5 Hydrogeochemistry – Monitoring of modern water at Erzberg revealed major spatial differences in the hydrochemical evolution for potential erzbergite formation. The local hydrochemical variations probably result from spatially (altitude and area) and seasonally variable meteoric water infiltration, fluid–solid interaction and mixing, distinct flow routes, as well as variable host rock dissolution and mineral precipitation in the aquifer. Most erzbergite samples originate from the more southern section of Erzberg which corresponds well to the measured water compositions. Hydrochemically, modern waters at Erzberg are still favourable for erzbergite formation irrespective of the anthropogenically disturbed chemical–sedimentary setting from the mining activities.

6 Fractures – The opening of fractures as a result of fault tectonic or gravitational mass movements is a prerequisite for the deposition of the aragonite–calcite veins, i.e. providing (vadose) water flow routes in the fissured aquifer (Fig. 9). Open fractures of particular width and length imply fresh chemical reaction surfaces of the host rock carbonates and sulphide accessories. Based on the hydrochemical mechanism of erzbergite formation and the results from U–Th dating, a young age and mostly short time intervals of fracture infilling are strongly supported. From a hydrogeochemical and structural point of view it seems unlikely that the fractures stay open over extended time intervals, i.e. most are of geologically young age too.

7 Climate archive – The erzbergite veins constitute a chemical–sedimentary archive for palaeoenvironmental (palaeoclimate) reconstructions. Erzbergite formation is favoured during relatively warm and wet climate intervals. The clumped and O isotopic compositions of CaCO₃ primarily depend on the prevailing past temperatures at Erzberg while the mineralogy/petrography, C isotopes and selected minor/trace elements have been shown to be most sensitive to regional meteoric precipitation.

ACKNOWLEDGEMENTS

Judith Jernej, Maria Hierz, Andrea Wolf and Sylvia Perchthold are acknowledged for their dedicated

work in the TU Graz laboratories. We would also like to thank Peter Sipos for performing preliminary μ -XRD analyses and Ralf Benischke for helpful discussions on the study site. Chemical and mineralogical analyses were conducted at the NAWI Graz Central Lab for Water, Minerals and Rocks as part of the NAWI Graz GeoCenter. Stable sulphur isotope ratios were measured by the Böttcher Lab at Leibniz IOW – I. Schmiedinger is thanked for invaluable mass spectrometric support. X. Wang and K. Lin were supported by a Singapore National Research Foundation Fellowship (NRFF2011-08 to X.W.). T. Kluge acknowledges support by the Heidelberg Graduate School of Fundamental Physics (HGSFP) and technical help of the team ‘Physics of Environmental Archives’ to maintain the IRMS instrument that was funded through the grant DFG-INST 35/1270-1. The VA Erzberg GmbH is acknowledged for research cooperation and access to the open pit mine. The critical suggestions of an anonymous reviewer and the dedicated suggestions of Alexander Brasier helped to improve this manuscript.

REFERENCES

- Angel, F. (1939) *Unser Erzberg. Mitt. Naturw. Ver. Steiermark*, **75**, 227–321.
- Bachan, A. and Kump, L.R. (2015) The rise of oxygen and siderite oxidation during the Lomagundi Event. *Proc. Natl Acad. Sci. USA*, **112**, 6562–6567.
- Bajo, P., Borsato, A., Drysdale, R., Hua, Q., Frisia, S., Zanchetta, G., Hellstrom, J. and Woodhead, J. (2017) Stalagmite carbon isotopes and dead carbon proportion (DCP) in a near-closed-system situation: an interplay between sulphuric and carbonic acid dissolution. *Geochim. Cosmochim. Acta*, **210**, 208–227.
- Baldermann, A., Deditius, A.P., Dietzel, M., Fichtner, V., Fischer, C., Hippler, D., Leis, A., Baldermann, C., Mavromatis, V., Stickler, C.P. and Strauss, H. (2015) The role of bacterial sulfate reduction during dolomite precipitation: implications from Upper Jurassic platform carbonates. *Chem. Geol.*, **412**, 1–14.
- Björck, S., Walker, M.J.C., Cwynar, L.C., Johnsen, S., Knudsen, K.-L., Lowe, J.J., Wohlfarth, B. and Members, I. (1998) An event stratigraphy for the Last Termination in the North Atlantic region based on the Greenland ice-core record: a proposal by the INTIMATE group. *J. Quatern. Sci.*, **13**, 283–292.
- Boch, R. and Spötl, C. (2011) Reconstructing palaeoprecipitation from an active cave flowstone. *J. Quatern. Sci.*, **26**, 675–687.
- Boch, R., Dietzel, M., Reichl, P., Leis, A., Baldermann, A., Mittermayr, F. and Pölt, P. (2015) Rapid ikaite (CaCO₃·6H₂O) crystallization in a man-made river bed: Hydrogeochemical monitoring of a rarely documented mineral formation. *Appl. Geochem.*, **63**, 366–379.
- Böttcher, M.E. and Dietzel, M. (2010) Metal-ion partitioning during low-temperature precipitation and dissolution of

- anhydrous carbonates and sulfates. *EMU Notes Mineral.*, **10**, 139–187.
- Bryda, G., van Husen, D., Kreuss, O., Koukal, V., Moser, M., Pavlik, W., Schönlaub, H.P. and Wagreich, M.** (2013) *Erläuterungen zu Blatt 101 Eisenarz - Geologische Karte der Republik Österreich 1:50000*. Geologische Bundesanstalt, Vienna, 223 pp.
- Busenberg, E. and Plummer, L.N.** (1985) Kinetic and thermodynamic factors controlling the distribution of SO_4^{2-} and Na^+ in calcites and selected aragonites. *Geochim. Cosmochim. Acta*, **49**, 713–725.
- Cheng, H., Edwards, R.L., Shen, C.-C., Polyak, V.J., Asmerom, Y., Woodhead, J., Hellstrom, J., Wang, Y., Kong, X., Spötl, C., Wang, X. and Alexander, E.C.** (2013) Improvements in ^{230}Th dating, ^{230}Th and ^{234}U half-life values, and U-Th isotopic measurements by multi-collector inductively coupled plasma mass spectrometry. *Earth Planet. Sci. Lett.*, **371–372**, 82–91.
- Daëron, M., Blamart, D., Peral, M. and Affek, H.P.** (2016) Absolute isotopic abundance ratios and the accuracy of Δ_{47} measurements. *Chem. Geol.*, **442**, 83–96.
- Deines, P., Langmuir, D. and Harmon, R.S.** (1974) Stable carbon isotope ratios and the existence of a gas phase in the evolution of carbonate ground waters. *Geochim. Cosmochim. Acta*, **38**, 1147–1164.
- Demény, A. and Siklósy, Z.** (2008) Combination of off-line preparation and continuous flow mass spectrometry: D/H analyses of inclusion waters. *Rapid Commun. Mass Sp.*, **22**, 1329–1334.
- Dennis, K.J., Affek, H.P., Passey, B.H., Schrag, D.P. and Eiler, J.W.** (2011) Defining an absolute reference frame for ‘clumped’ isotope studies of CO_2 . *Geochim. Cosmochim. Acta*, **75**, 7117–7131.
- Dietzel, M., Gussone, N. and Eisenhauer, A.** (2004) Coprecipitation of Sr^{2+} and Ba^{2+} with aragonite by membrane diffusion of CO_2 between 10 and 50°C. *Chem. Geol.*, **203**, 139–151.
- Dietzel, M., Schön, F., Heinrichs, J., Deditius, A.P. and Leis, A.** (2015) Tracing formation and durability of calcite in a Punic-Roman cistern mortar (Pantelleria Island, Italy). *Isotopes Environ. Health Stud.*, **52**, 112–127.
- Drysdale, R., Zanchetta, G., Hellstrom, J., Maas, R., Fallick, A., Pickett, M., Cartwright, I. and Piccini, L.** (2006) Late Holocene drought responsible for the collapse of Old World civilizations is recorded in an Italian cave flowstone. *Geology*, **34**, 101–104.
- Dublyansky, Y.V. and Spötl, C.** (2009) Hydrogen and oxygen isotopes of water from inclusions in minerals: design of a new crushing system and on-line continuous-flow isotope ratio mass spectrometric analysis. *Rapid Commun. Mass Sp.*, **23**, 2605–2613.
- Eiler, J.M.** (2007) ‘Clumped-isotope’ geochemistry—The study of naturally-occurring, multiply-substituted isotopologues. *Earth Planet. Sci. Lett.*, **262**, 309–327.
- Fairchild, I.J., Smith, C.L., Baker, A., Fuller, L., Spötl, C., Matthey, D., McDermott, F. and Facility, E.I.M.** (2006) Modification and preservation of environmental signals in speleothems. *Earth-Sci. Rev.*, **75**, 105–153.
- Frisia, S.** (2015) Microstratigraphic logging of calcite fabrics in speleothems as tool for palaeoclimate studies. *Int. J. Speleol.*, **44**, 1–16.
- Frisia, S., Borsato, A., Fairchild, I.J., McDermott, F. and Selmo, E.M.** (2002) Aragonite-calcite relationships in speleothems (Grotte De Clamouse, France): environment, fabrics, and carbonate geochemistry. *J. Sediment. Res.*, **72**, 687–699.
- Goldsmith, J.R., Graf, D.L. and Heard, H.C.** (1961) Lattice constants of the calcium-magnesium carbonates. *Am. Mineral.*, **46**, 453–457.
- Hager, B. and Foelsche, U.** (2015) Stable isotope composition of precipitation in Austria. *Austrian J. Earth Sci.*, **108**, 2–13.
- Hanshaw, B.B. and Back, W.** (1979) Major geochemical processes in the evolution of carbonate–aquifer systems. *J. Hydrol.*, **43**, 287–312.
- Hatle, E.** (1892) Fünfter Beitrag zur mineralogischen Topographie der Steiermark. *Mitt. Naturw. Ver. Steiermark*, **28**, 294–308.
- Hoefs, J.** (2015) *Stable Isotope Geochemistry*. Berlin Heidelberg, Springer, 389 pp.
- Horita, J., Ueda, A., Mizukami, K. and Takatori, I.** (1989) Automatic δD and $\delta^{18}\text{O}$ analyses of multi-water samples using H_2 - and CO_2 -water equilibration methods with a common equilibration set-up. *Int. J. Radiat. Appl. Instr. Part A. Appl. Radiat. Isot.*, **40**, 801–805.
- Huang, Y. and Fairchild, I.J.** (2001) Partitioning of Sr^{2+} and Mg^{2+} into calcite under karst-analogue experimental conditions. *Geochim. Cosmochim. Acta*, **65**, 47–62.
- Huntington, K.W. and Lechler, A.R.** (2015) Carbonate clumped isotope thermometry in continental tectonics. *Tectonophysics*, **647/648**, 1–20.
- Jaffey, A.H., Flynn, K.F., Glendenin, L.E., Bentley, W.C. and Essling, A.M.** (1971) Precision measurement of half-lives and specific activities of ^{235}U and ^{238}U . *Phys. Rev. C*, **4**, 1889–1906.
- Jones, B.** (2017) Review of calcium carbonate polymorph precipitation in spring systems. *Sed. Geol.*, **353**, 64–75.
- Kendall, A.C. and Broughton, P.L.** (1978) Origin of fabrics in speleothems composed of columnar calcite crystals. *J. Sed. Petrol.*, **48**, 519–538.
- Kim, S.-T., O’Neil, J.R., Hillaire-Marcel, C. and Mucci, A.** (2007) Oxygen isotope fractionation between synthetic aragonite and water: influence of temperature and Mg^{2+} concentration. *Geochim. Cosmochim. Acta*, **71**, 4704–4715.
- Kim, S.-T., Coplen, T.B. and Horita, J.** (2015) Normalization of stable isotope data for carbonate minerals: implementation of IUPAC guidelines. *Geochim. Cosmochim. Acta*, **158**, 276–289.
- Kluge, T., John, C.M., Jourdan, A.-L., Davis, S. and Crawshaw, J.** (2015) Laboratory calibration of the calcium carbonate clumped isotope thermometer in the 25–250 °C temperature range. *Geochim. Cosmochim. Acta*, **157**, 213–227.
- Koltai, G., Spötl, C., Luetscher, M., Cheng, H., Barrett, S.J. and Müller, W.** (2017) The nature of annual lamination in carbonate flowstones from non-karstic fractures, Vinschgau (northern Italy). *Chem. Geol.*, **457**, 1–14.
- Lachniet, M.S., Bernal, J.P., Asmerom, Y. and Polyak, V.** (2012) Uranium loss and aragonite–calcite age discordance in a calcitized aragonite stalagmite. *Quatern. Geochronol.*, **14**, 26–37.
- Lisiecki, L.E. and Raymo, M.E.** (2005) A Pliocene–Pleistocene stack of 57 globally distributed benthic $\delta^{18}\text{O}$ records. *Paleoceanography*, **20**, PA1003. <https://doi.org/10.1029/2004PA001071>.
- Mann, J.L., Vocke, R.D. and Kelly, W.R.** (2009) Revised $\delta^{34}\text{S}$ reference values for IAEA sulfur isotope reference materials S-2 and S-3. *Rapid Commun. Mass Sp.*, **23**, 1116–1124.
- Meyer, M.C., Cliff, R.A. and Spötl, C.** (2011) Speleothems and mountain uplift. *Geology*, **39**, 447–450.

- Michaelis, J., Usdowski, E. and Menschel, G. (1985) Partitioning of ^{13}C and ^{12}C on the degassing of CO_2 and the precipitation of calcite; Rayleigh-type fractionation and a kinetic model. *Am. J. Sci.*, **285**, 318–327.
- Mickler, P.J., Stern, L.A. and Banner, J.L. (2006) Large kinetic isotope effects in modern speleothems. *Geol. Soc. Am. Bull.*, **118**, 65–81.
- Mittermayr, F., Bauer, C., Klammer, D., Böttcher, M.E., Leis, A., Escher, P. and Dietzel, M. (2012) Concrete under Sulphate Attack: an Isotope Study on Sulphur Sources. *Isotopes Environ. Health Stud.*, **48**, 105–117.
- Mittermayr, F., Baldermann, A., Baldermann, C., Grathoff, G.H., Klammer, D., Köhler, S.J., Leis, A., Warr, L.N. and Dietzel, M. (2017) Environmental controls and reaction pathways of coupled de-dolomitization and thaumasite formation. *Cement Concrete Res.*, **95**, 282–293.
- Morrison, J., Brockwell, T., Merren, T., Fourel, F. and Phillips, A.M. (2001) On-line high-precision stable hydrogen isotopic analyses on nanoliter water samples. *Anal. Chem.*, **73**, 3570–3575.
- Morse, J.W. and Mackenzie, F.T. (1990) *Geochemistry of Sedimentary Carbonates. Developments in Sedimentology*. Elsevier Science, Amsterdam, The Netherlands, 706 pp.
- Niedermayr, A., Köhler, S.J. and Dietzel, M. (2013) Impacts of aqueous carbonate accumulation rate, magnesium and polyaspartic acid on calcium carbonate formation (6–40°C). *Chem. Geol.*, **340**, 105–120.
- Onuk, P., Dietzel, M. and Hauzenberger, C.A. (2014) Formation of helictite in the cave Dragon Belly (Sardinia, Italy)—Microstructure and incorporation of Mg, Sr, and Ba. *Chem. Erde. Geochem.*, **74**, 443–452.
- Ortega, R., Maire, R., Devès, G. and Quinif, Y. (2005) High-resolution mapping of uranium and other trace elements in recrystallized aragonite–calcite speleothems from caves in the Pyrenees (France): implication for U-series dating. *Earth Planet. Sci. Lett.*, **237**, 911–923.
- Parkhurst, D.L. and Appelo, C.A.J. (2013) Description of input and examples for PHREEQC version 3—a computer program for speciation, batch-reaction, one-dimensional transport, and inverse geochemical calculations. *US Geol. Surv. Tech. Methods*, **6**, A43, 497.
- Pirajno, F. (2009) *Hydrothermal Processes and Mineral Systems*. Springer, the Netherlands, 1250 pp.
- Prochaska, W. (2012) Siderite and magnesite mineralizations in Palaeozoic strata of the Eastern Alps (Austria). *J. Alpine Geol.*, **54**, 309–322.
- Prochaska, W. (2016) Genetic concepts on the formation of the Austrian magnesite and siderite mineralizations in the Eastern Alps of Austria. *Geol. Croatica*, **69**, 31–38.
- Purgstaller, B., Dietzel, M., Baldermann, A. and Mavromatis, V. (2017) Control of temperature and aqueous $\text{Mg}^{2+}/\text{Ca}^{2+}$ ratio on the (trans-)formation of ikaite. *Geochim. Cosmochim. Acta*, **217**, 128–143.
- Riechelmann, S., Schröder-Ritzrau, A., Wassenburg, J.A., Schreuer, J., Richter, D.K., Riechelmann, D.F.C., Terente, M., Constantin, S., Mangini, A. and Immenhauser, A. (2014) Physicochemical characteristics of drip waters: influence on mineralogy and crystal morphology of recent cave carbonate precipitates. *Geochim. Cosmochim. Acta*, **145**, 13–29.
- Rodriguez-Navarro, C. and Benning, L.G. (2013) Control of crystal nucleation and growth by additives. *Elements*, **9**, 203–209.
- Rosenbaum, J. and Sheppard, S.M.F. (1986) An isotopic study of siderites, dolomites and ankerites at high temperatures. *Geochim. Cosmochim. Acta*, **50**, 1147–1150.
- Rossi, C. and Lozano, R.P. (2016) Hydrochemical controls on aragonite versus calcite precipitation in cave dripwaters. *Geochim. Cosmochim. Acta*, **192**, 70–96.
- Schmid, S.M., Fügenschuh, B., Kissling, E. and Schuster, R. (2004) Tectonic map and overall architecture of the Alpine orogen. *Eclogae Geol. Helv.*, **97**, 93–117.
- Scholz, D., Mühlinghaus, C. and Mangini, A. (2009) Modelling $\delta^{13}\text{C}$ and $\delta^{18}\text{O}$ in the solution layer on stalagmite surfaces. *Geochim. Cosmochim. Acta*, **73**, 2592–2602.
- Schönlaub, H.-P. (1982) Die Grauwackenzone in den Eisenerzer Alpen (Österreich). *Jahrb. Geol. B.-A.*, **124**, 361–423.
- Schulz, O., Vavtar, F. and Dieber, K. (1997) Die Siderit-Erzlagerstätte Steirischer Erzberg: Eine geowissenschaftliche Studie, mit wirtschaftlicher und geschichtlicher Betrachtung. *Arch. Lagerst. Forsch. Geol. B.-A.*, **20**, 65–178.
- Shen, C.-C., Wu, C.-C., Cheng, H., Edwards, R.L., Hsieh, Y.-T., Gallet, S., Chang, C.-C., Li, T.-Y., Lam, D.D., Kano, A., Hori, M. and Spötl, C. (2012) High-precision and high-resolution carbonate ^{230}Th dating by MC-ICP-MS with SEM protocols. *Geochim. Cosmochim. Acta*, **99**, 71–86.
- Spötl, C. (2005) A robust and fast method of sampling and analysis of $\delta^{13}\text{C}$ of dissolved inorganic carbon in ground waters. *Isotopes Environ. Health Stud.*, **41**, 217–221.
- Spötl, C. and Matthey, D. (2006) Stable isotope microsampling of speleothems for palaeoenvironmental studies: a comparison of microdrill, micromill and laser ablation techniques. *Chem. Geol.*, **235**, 48–58.
- Spötl, C., Fohlmeister, J., Cheng, H. and Boch, R. (2016) Modern aragonite formation at near-freezing conditions in an alpine cave, Carnic Alps, Austria. *Chem. Geol.*, **435**, 60–70.
- Strauhel, T., Prager, C., Millen, B., Spötl, C., Zangerl, C. and Brandner, R. (2016) Aquifer geochemistry of crystalline rocks and Quaternary deposits in a high altitude alpine environment (Kauner Valley, Austria). *Austrian J. Earth Sci.*, **109**, 29–44.
- Thalmann, F. (1979) Zur Eisenspatvererzung in der nördlichen Grauwackenzone am Beispiel des Erzberges bei Eisenerz und Radmer/Bucheck. *Verh. Geol. B.-A.*, **3**, 479–489.
- Umweltbundesamt (2017) *H₂O Fachdatenbank*. Available at: <https://wasser.umweltbundesamt.at/h2odb/> (last accessed 29 June 2018).
- Wang, X., Edwards, R.L., Auler, A.S., Cheng, H., Kong, X., Wang, Y., Cruz, F.W., Dorale, J.A. and Chiang, H.-W. (2017) Hydroclimate changes across the Amazon lowlands over the past 45,000 years. *Nature*, **541**, 204–207.
- Wassenburg, J.A., Scholz, D., Jochum, K.P., Cheng, H., Oster, J., Immenhauser, A., Richter, D.K., Häger, T., Jamieson, R.A., Baldini, J.U.L., Hoffmann, D. and Breitenbach, S.F.M. (2016) Determination of aragonite trace element distribution coefficients from speleothem calcite–aragonite transitions. *Geochim. Cosmochim. Acta*, **190**, 347–367.
- Weber, L. (1997) Handbuch der Lagerstätten der Erze, Industriemineralien und Energierohstoffe Österreichs. *Arch. Lagerst. Forsch. Geol. B.-A.*, **19**, 1–607.
- Winde, V., Böttcher, M.E., Voss, M. and Mahler, A. (2017) Bladder wrack (*Fucus vesiculosus*) as an environmental bio-monitor in an urbanized fjord of the western Baltic Sea. *Isotopes Environ. Health Stud.*, **53**, 1–17.
- Zhou, G.-T. and Zheng, Y.-F. (2003) An experimental study of oxygen isotope fractionation between inorganically precipitated aragonite and water at low temperatures. *Geochim. Cosmochim. Acta*, **67**, 387–399.

Manuscript received 20 September 2017; revision accepted 24 May 2018

Supporting Information

Additional Supporting Information may be found in the online version of this article:

Figure S1. Additional transmitted light (TL) and reflected light (RL) photomicrographs showing petrographic details of erzbergite samples.

Figure S2. Additional hydrochemical relationships of modern waters at Erzberg plotting spatial differences as well as similarities between more southern, central and northern sampling sites.

Table S1. Powder X-ray diffraction analyses of various erzbergite and host rock subsamples for semi-quantitative determination of major and minor mineralogical compositions.

Table S2. Typical erzbergite precipitation (growth) rates calculated from selected precisely dated subsamples.

Table S3. Stable C and O isotope data of different carbonates from the Erzberg mine; EB – erzbergite precipitates in fractures, siderite, ankerite and Sauberger Kalk limestone calcite.

Table S4. Stable C and O isotope analyses from a continuous (milled at 1 mm spatial resolution) isotope transect of erzbergite sample EB2.

Table S5. Mass spectrometric measurement results and calibration data for clumped isotope temperature calculation.